1 2 9 0

UNIVERSIDADE Ð
COIMBRA

MUHAMMAD ANS

DEVELOPMENT OF CORROSION AND WEAR RESISTANT COATINGS FOR MARITIME APPLICATIONS DEPOSITED BY HiPIMS/DOMS

VOLUME 1

Dissertation under the Joint European Master's Degree in Surface Tribology and Interfaces guided by Prof. Sandra Carvalho and Jose David Castro presented to the Department of Mechanical Engineering of the Faculty of Science and Technology of the University of Coimbra.

July 2022

Development of corrosion and wear resistant coatings for maritime applications deposited by HiPIMS/DOMS

Submitted in Partial Fulfilment of the Requirements for the Degree of European Joint European Master in Tribology of Surfaces and Interfaces.

Desenvolvimento de revestimentos resistentes à corrosão e ao desgaste para aplicações marítimas depositado por HiPIMS/DOMS

Author

Muhammad ANS

Advisors

Prof. Sandra Carvalho

Jose David Castro

Jury

President	**Professor Bruno Trindade**
	Professor at the Universidade de Coimbra
Vowel	**Doutor Todor Vuchkov**
	Researcher at Instituto Pedro Nunes
Advisor	**Professor Sandra Carvalho**
	Professor at Universidade de Coimbra

Coimbra, July, 2022

ACKNOWLEDGEMENTS

First and foremost, I would like to convey my deepest gratitude towards my supervisor **Prof. Sandra Carvalho** Professor at Department of Mechanical Engineering, Universidade de Coimbra for her guidance, support and advice throughout my thesis work.

In particular I would like to thank my co-supervisor Jose David Castro PhD researcher at Universidade de Coimbra. Without his guidance it was not possible to prepare samples and deposition also he taught me theoretical knowledge regarding the research work. I must mention special thanks to Ms. Beatriz Pinto for her help in experimental activity.

My sincere thanks for **Prof. Bruno Trindade**, head of our master's degree at Universidade de Coimbra who helped me when I first arrived in Portugal. He guided me in every critical situation, I truly want to appreciate his sympathy during my study period.

My heartiest gratitude for TRIBOS+ and its consortium Universities (University of Leeds, University of Ljubljana and Lulea Technical University) to provide me an opportunity during my M.Sc degree and chance to perform research activities. My special gratitude for Dr. Ksenija Neumann from Aachen-RWTH, Germany for providing an internship of three months during the summer break. It was a great platform by which I could enhance my research skills to next level. I would like to say many thanks my all teachers and professors from all TRIBOS partner universities and my classmates for helping me occasionally in many areas. It was pleasure to meet them and had great company. Special thanks to my best friend Anzum Al Abir.

Last but not least I would also like to take this opportunity to thanks my parents especially my mother who was always there to support me, my elder and younger sisters, my brother and all other friends and family members in Pakistan.

ABSTRACT

Zirconium nitride (ZrN) coatings were obtained *via* deep oscillation magnetron sputtering (DOMS) and direct current magnetron sputtering (DCMS) on 316L stainless steel substrate for potential use in sea chest gratings, part broadly used in ships. The effect of N_2 flow and working pressure on the properties of the coatings were investigated in the deposition chamber. The corrosion behaviour was evaluated in 3.5% NaCl solution through the electrochemical impedance spectroscopy (EIS) and potentiodynamic polarization tests. The tribological analysis was determined in dry and wet (3.5% NaCl) conditions using the pin-on-disc test. The results showed that the coatings obtained by DOMS technology were dense and compact. Furthermore, the EIS measurements reported a higher impedance on the coatings deposited *via* the DOMS technique (80% N_2 flow at 0.4 Pa working pressure). Similarly, the least I_{corr} and corrosion rates were achieved for 72 h of immersion time for the same coating. However, the coefficient of friction (COF) and wear rates of DOMS-coated samples were lower than DCMS-coated and uncoated samples in both dry and wet conditions.

Keywords: ZrN coatings, DOMS deposition, Corrosion behaviour, Tribological analysis

RESUMO

Revestimentos de nitreto de zircónio (ZrN) foram obtidos através Deposição catódica com impulsos de alta potência (*Deep Oscillations Magnetron Sputtering* – DOMS) e pulverizaçãocatódica em magnetrão em corrente contínua (DCMS) em substratos de aço inoxidável 316L para uso potencial em grades de caixa de mar, parte amplamente utilizada em navios. Neste trabalho estudou-se o efeito do fluxo de N_2 e consequentemente da pressão de trabalho, bem como a fonte de tensão aplicada, nas propriedades funcionais do revestimentos desenvolvidos. A resistência à corrosão foi avaliada em 3.5% de NaCl por meio de espectroscopia de impedância eletroquímica (EIS) e ensaios de polarização potenciodinâmica. A caraterização tribológica foi realizada utilizando o teste pino-disco, sem lubrificação e em ambiente salino (3.5% NaCl). Os resultados mostraram que os revestimentos obtidos pela tecnologia DOMS eram densos e compactos. Além disso, as medições EIS relataram uma maior impedância nos revestimentos depositados através da técnica DOMS (80% de fluxo de N_2 a 0.4 Pa de pressão de trabalho). Da mesma forma, as menores taxas de Icorr e corrosão foram alcançadas para 72 h de tempo de imersão para o mesmo revestimento. Todavia, o coeficiente de atrito e de desgaste das amostras revestidas a DOMS foi obtido inferior às amostras revestidas a DCMS e não revestidas.

Palavras-chave: Revestimentos ZrN, Deposição DOMS, Comportamento à corrosão, Análise tribológica

CONTENTS

LIST OF FIGURES

LIST OF TABLES

LIST OF SYMBOLS

^{o}C – Degree Celsius

μm – micrometer

Ω – Ohm

θ – Theta

kHz – Kilo Hertz

W – Watt

V – Volt

H – Hydrogen

Cl^{-}– Chloride ions

Zr – Zirconium

N – Nitrogen

C – Carbon

Ni – Nickel

Fe – Iron

Cr – Chromium

Mg – Magnesium

Ar – Argon

P – Phosphorous

Co – Cobalt

Si – Silicon

Mo – Molybdenum

O – Oxygen

Ag – Silver

LIST OF ACRONYMS/ ABBREVIATIONS

HiPIMS – High power impulse magnetron sputtering

DOMS – Deep oscillation magnetron sputtering

DCMS – Direct current magnetron sputtering

AISI – American iron and steel institute

ZrN – Zirconium nitride

ZrO – Zirconium oxide

ZnO – Zinc oxide

TiO – Titanium oxide

DLC – Diamond like carbon

SEM – Scanning electron microscopy

EIS – Electrochemical impedance spectroscopy

XRD – X-ray diffraction

SiO_2 – Silicon dioxide

Al_2O_3 – Alumina

PVD – Physical vapour deposition

CVD – Chemical vapour deposition

e.g. – Exempli gratia

i.e. – id est

VC – Vanadium carbide

TiN – Titanium nitride

RF – Radio frequency

ZrCN – Zirconium carbon nitride

SCE – Saturated calomel electrode

SZD – Structure zone diagram

CHAPTER 1

1. INTRODUCTION

Corrosion of steel in the marine atmosphere becomes serious because of its extremely corrosive nature and presence of high salinity in seawater [1]. The research of corrosion protection mechanisms in seawater is very meaningful. Several useful techniques have been studied to coat the surface of steel with protective coatings, such as nickel phosphate (Ni-P) coating, ceramic coating, glass coating, and superhydrophobic film [2]. With regards to the Ni-P coating, it is generally applied *via* electroless deposition (a reaction between Ni^{2+} and $H_2PO_2^-$) to achieve the corrosion-resistant coating on carbon steel substances at a micro-scale. However, hydrogen escapes through the pores induced during the preparing process making it less effective.

Recently, some oxide ceramic coatings have been reported in the literature, such as SiO_2 [3], Al_2O_3 [4], TiO_2 [5] and ZrO_2 [6], which provide insulation, heat resistance and corrosion resistance for several applications. TiO_2 coating has a great shielding ability with high impedance. The coating applied *via* sol-gel technique; somewhat gel decomposes at high temperature causes surface cracks. These cracks allow corrosive seawater penetration through the coatings and directly interact with the steel surface, causing the occurrence of serious corrosion at the substrate interface. To decrease the number of cracks, a small amount of ZrO nanoparticles has been added to produce TiO_2/ZrO composite [7]. The results showed that anticorrosion ability has been substantially obtained for the coating. However, such ceramic film is still under consideration to further develop its anticorrosion goal. Furthermore, tribological performance and mechanical properties of zirconium nitride (ZrN) coatings can be significantly enhanced most notably in harsh environments. Of particular, these properties resulting nanostructured protective coatings of appropriate choice against wear resistance on the steel substrate [8, 9].

Deep oscillation magnetron sputtering (DOMS), owing to its high peak power density, high-ion flux and high peak power density is well-known modern physical vapour deposition (PVD) technique that allows high-quality thin films deposition [10]. DOMS has expanded the area of applications for growing excellent quality thin films with smoother morphology, higher hardness, better adhesion, and denser structure properties in comparison

to conventional magnetron sputtering. This technique has greatly considered research attention from an industrial viewpoint due to its potential maritime applications and wear-resistance coatings. Various functional thin films have been coated *via* DOMS, such as TiO_x, ZrO_2, and diamond-like carbon (DLC) [11, 12].

In the light of the above literature survey, all these single/multilayers cannot offer steel substrate with suitable protection from seawater attack due to intrinsic flaws (small cracks and pores) [13]. As a matter of fact, the excellent properties of steel substrate are not discarded and enables the material to have desirable corrosion resistance in seawater, a new method is introduced to produce a hard wear-resistant coating. Herein, we have demonstrated a dense structured ceramic-based film (i.e., ZrN) onto 316L stainless steel substrate using the DOMS technique. A further investigation on corrosion behaviour of hard wear-resistant coating have been examined using electrochemical methods, such as potentiodynamic polarization and electrochemical impedance spectroscopy (EIS) measurements. Further morphology and crystal structure formed on the coating have explored with the aid of fundamental characterization techniques, e.g., Scanning Electron Microscopy (SEM), and X-ray Diffraction (XRD).

1.1. Objective of the thesis

The main objective of this work was to study the ZrN based coatings using the DOMS and direct current magnetron sputtering (DCMS). The deposition process was carried out under optimized conditions to attain desired dense morphology, capable to work in the marine environment. The ZrN films were applied on stainless steel (SS) and silicon substrates to achieve reliable mechanical behaviour (i.e., wear-resistant) and anti-corrosion properties. To accomplish the main goal, the following aspects of research were considered:

- Optimised the deposition parameters to achieve excellent mechanical and corrosion resistant properties.

- Adequate analysis technique to examine the physical, mechanical and chemical properties of the coatings. A suitable environment to access the anti-corrosion and wear resistant properties of the hard coatings.

- In order to establish high resistance coatings with enhanced mechanical properties, the concentration of N_2 at different voltages were varied for this research.

CHAPTER 2

2. THEORETICAL BACKGROUND

In this chapter, the properties of stainless steel coated with various effective coatings are explained in detail. The structure, morphology, and mechanical properties of coatings implemented by researchers and what is their industrial relevancy is described. The thin-film techniques employed for deposition in various optimized parameters are also explained briefly. Corrosion and oxidation behaviour along with their fundamental applications specifically for ZrN coatings have been elaborated.

2.1. The effect of seawater on corrosion behaviour

The corrosion behaviour of metals in seawater is affected by the environmental variables associated with specific marine applications. Among the more influential of these factors are temperature, dissolved oxygen content and high amount of chloride species in the water. It is difficult to separate the effects of these variables in nature seawater because of the dissolved harmful species (Cl^-, SO_4^{2-}) in it [14]. Corrosion of metals in seawater desalination systems includes both general and localized corrosion. Concerning the involvement of sliding components in different engineering disciplines makes wear-resistance an important aspect to ensure the reliability of these components. Both corrosion behaviour and wear-resistance bring great harm to the service life of seawater desalination equipment and safe operation of the system. Corrosion in the seawater leads to significant economic losses, such as loss of production, loss of product, loss of efficiency and product contamination. Even more serious, it leads to catastrophic major accidents, such as leakage of toxic substances, causing environmental pollution, endangering people's health [15].

2.2. The main influencing factors of corrosion and wear on stainless steel

During the last few decades, there has been extensive progress in understanding the behaviour of stainless steel in seawater. The problem of corrosion in seawater is very

common at the industrial level for maritime applications. In order to ensure long-term safe operation of equipment, reasonable selection of material is the most important aspect. It is necessary to consider the process conditions, but also consider the materials structure, properties and the changes during the use process. Stainless steel is one of the best alternatives compared to chromium and titanium alloys due to cost effectiveness and corrosion resistance properties. The presence of chromium in steel forms a self-repairing passive layer of chromium oxide on the surface that increases the oxidation and corrosion resistance [16]. The general chemical composition of stainless steel used in marine applications is given in *Table 2.1*. In a seawater environment, the pumps, open hydraulic drive system and blades of ships are exposed to seawater during the running of the machine [17]. In this case, liquid lubricants do not provide a full lubricating effect due to the leakage of oil and the highly corrosive nature of seawater. The mechanical parts are required to have great wear and corrosion-resistant properties in seawater in order to extend service life and reduce the cost of maintenance of parts. The progress of improving properties is accomplished through modification in the thermal treatments of the steel, chemical composition, and mechanical behaviours [18]. Despite excellent mechanical properties, the corrosion and oxidation resistance of stainless steel needs to be enhanced to ensure long-term durability. However, the quality of stainless steel could be compromised in exposure to seawater, once the corrosion process begins it brings the loss of mechanical properties as a consequence of the deterioration of the outer surface. Moreover, it may cause the loss of alloying elements that affect its performance in industrial applications [19, 20].

To enhance the surface properties of stainless steel, ceramic coatings can be applied, and surface chemistry can be altered, due to this concept, research in ceramic thin films and coatings constituents is an area of development because they offer an outstanding choice for protecting steel in seawater. The ceramic layer prevents the corrosion mechanism of Cl^- from attacking the steel surface and improving the mechanical properties such as wear-resistance and hardness [21, 22].

Table 2.1: Chemical composition of stainless-steel [16]

Elements	Fe	Cr	Ni	Mn	Mo	Si	C	P	Cu	Co	V
Wt.%	69.9	17.7	7.9	1.75	0.32	0.015	0.025	0.03	0.84	0.17	0.1

2.3. Coatings

A coating is a covering that is applied to the surface of an object, usually referred to as the substrate. Several coatings and a full range of application techniques produce unique performance characteristics, such as anti-corrosion, thermal oxidation, chemical and wear resistance. Paint is another example that is extensively used to protect the surface. Marine paints are most commonly used to coat the exterior surface of big ships, boats, vessels tankers, etc [23]. However, with constant exposure to seawater, these paints cannot resist for long. The development of effective pre-treatments for metallic substrates has attracted a lot of attention, owing to their ability to increase the durability of metal structures and components in aggressive environments (e.g., NaCl, alkaline media, and marine water) and wear conditions [16, 24, 25].

2.3.1. ZrO_2 coatings

ZrO_2 coatings are very interesting because of their excellent mechanical, thermal, optical and electrical properties [6]. ZrO_2 reveals excellent properties such as high strength, high fracture toughness, wear resistance and chemical and corrosion resistance [26] in comparison to ordinary paints. Wang et al. prepared Ni–ZrO_2 nanocomposite coatings by direct current (DC) electrodeposition and concluded that co-deposited ZrO_2 improved the microhardness, wear and frictional and corrosion resistance properties of the metal matrix [27]. Briefly, the authors produced uniform ZnO_2 coatings on steel substrate and characterized the corrosion resistance properties using electrochemical testing in 3.5 wt% NaCl solution. The open-circuit potential showed the more negative potential of the coated samples compared to the bare substrate. This implies that the composite coating developed a more noble character and hinders the anodic reaction, which possesses anti-corrosion properties. Setiawan et al. [28] coated ZrO_2 nanocomposite coatings using the sputtering technique and studied the variation of nanoparticles in composite. The morphology and microhardness results showed a high wear and erosion resistance coating.

2.3.2. ZrN coatings

The transition metal nitride coatings have excellent properties, such as high hardness, good wear resistance, chemical stability, corrosion resistance and attractive colors. They, therefore, are widely used in industry in the current decade [29]. ZrN has an fcc structure and exhibits covalent bonding due to interactions between the 2p state of the N and the 4d state of Zr, resulting in Zr–N and Zr–Zr bonding but no N–N bonding. ZrN can accommodate non-metal vacancies [30]. More recently, ZrN started to attract more attention for its corrosion resistance, mechanical properties and warmly golden colour, compared to the corresponding properties of TiN film [31]. Furthermore, due to its wettability, ZrN is the best option among other nitrides to avoid corrosion problems in the presence of anion-based ionic liquids (containing hydroxyl and carboxyl bonds) [32].

Staia et al. [11] investigated the behaviour of ZrN coatings of 3.2–6.2 μm thickness deposited on an AISI M2 steel by magnetron sputtering. Wear testing was carried out under potentiostatic control in an artificial sweat solution. The authors reported that the amount of material removed and the time needed for the film to be released from the contact zone depend on the coating thickness. Moreover, it was determined that the substrate's dissolution governed the coated system's degradation.

2.3.3. Corrosion resistance ZrN_xO_y coatings

Zirconium oxynitride (ZrN_xO_y) coatings come across in a broad range of thermal applications [33]. According to recent research, the performance of these oxynitrides is determined not only by the deposition method, but also by the concentration and distribution of the N_2 atoms integrated into the matrix [34, 35]. Ariza et al. [35] investigated single-layered ZrN_xO_y thin films using RF magnetron sputtering technique at 300 °C. The obtained results showed that by varying O/N ratios, corrosion resistance improved by the influence of O_2. Moreover, the coatings contributed good impedance characteristics of the film/solution, film/adhesion layer and adhesion layer/substrate interfaces. Undoubtedly, the most crucial characteristic is corrosion protection in comparison with other ceramic materials. However, depending on the optimum conditions and applications in the marine environment which

sometimes leads to coating deteriorates by an acceleration of corrosion. There is a still gap of optimized deposition on steel substrate which needs to be studied thoroughly.

2.3.4. Corrosion, oxidation, and erosion resistance behaviour of ZrN/ZrO₂

The oxidation and corrosion behaviour of ZrN coatings was studied and compared at 600 $^{\circ}$C in water vapour and the air [8]. *Figure 2.1* shows that the oxide layer of ZrN increased drastically in steam (vapour) as a function of time. Because of the huge pores, the parabolic oxidation rate of ZrN in water vapour was two orders of magnitude faster. As a result, a dense network of fissures emerged across the ZrO_2 layer. A tetragonal bilayered structure of ZrO_2 (near the interface) toward the outer surface originated. Across the scale, the lateral cracks were formed because of volume expansion while tetragonal to monoclinic transition. It has been proposed that stabilisation of the ZrO_2 (tetragonal) phase could result in a denser scale, which would provide greater protection for Zr cladding utilised in nuclear reactor applications.
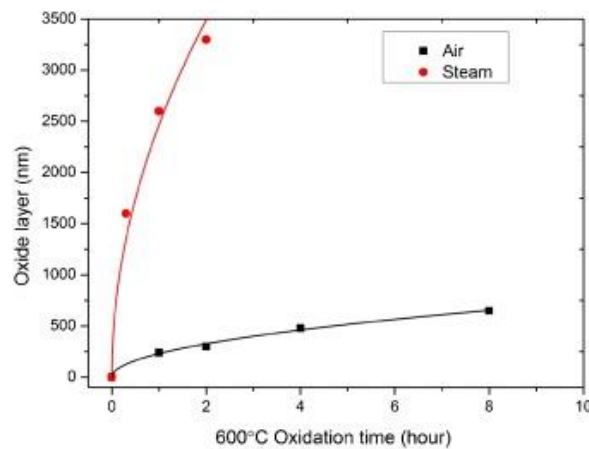
Figure 2.1: *Oxide thickness plot of ZrN as a function of time measured at 600 $^{\circ}$C in air and water vapour [8].*

Using plasma sputtering, ZrN coatings were deposited on titanium alloy compressor blades [36]. The results showed fair corrosion resistance with no reduction in the substrate's fatigue strength and tensile properties. Coatings increased resistance to gas abrasive wear by 25-35 times. As a result, such coatings were appropriate for usage on gas turbine engine parts and blades. ZrN film erosion was controlled by plasticity and brittle fracture up to 540

^{o}C when applied using the arc evaporation procedure and tested at 90 ^{o}C [37]. However, after 540 ^{o}C, the increase in erosion rate was ascribed to the reduction of compressive residual stresses in the coatings.

Various coatings were deposited using the ion-plasma technique, including VC, TiN, VN, and Cr_3C_2, in the thickness range of 15-30 μm. These coatings were tested for gas-abrasive wear resistance with sand particles containing 250-300 μm. [9]. The performance of ZrN coating was discovered to be most effective in protecting steel compressor blades.

2.3.5.   Microstructure of Zr-nitride coatings

Due to wear behaviour, a microstructural study of coatings is crucial. Process parameters of deposition, i.e., rate of deposition, chemical composition, voltage, and temperature, greatly influenced the microstructure. Fine and dense grains lower the columnar morphology while low deposition rates cause smoother layers. In addition, columnar morphology play an essential role in corrosion resistance and hardness [38, 39].

Roman et al. [40] have studied the microstructure growth (see *Figure 2.2*) of ZrN film produced *via* the magnetron technique. *Figure 2.2* (top) shows a cross-section of a thin film. The thin film was deposited at 500 ^{o}C for 60 minutes at a partial pressure of N_2 of 1.0 x 10$^-$^{3} m bar. A thin film of roughly 790 nm is readily visible (outermost layer) over the substrate in the sample. The film has a columnar morphology, indicating that the growth process preferentially progresses perpendicular to the surface plane of the substrate. For different N_2 partial pressures, the phase analysis of thin ZrN films was explored using XRD (*Figure 2.2* bottom). The diffraction lines are attributable to the ZrN phase, with minor peaks due to the Si substrate. As can be observed, the intensity of the ZrN phase peaks increases as the N_2 partial pressure decreases. These findings support the observed deposition rate and film thickness for various N_2 partial pressures. Clearly, the intensity of peaks uprising by increasing crystalline phase concentration. These results corresponding to the deposition rate and thickness of the coating obtained at different N_2 flow. The deposition rate is slower at higher N_2 flow which results in low film thickness. The diffraction patterns (see *Figure 2.2*) for thicker films are more intense but, they show low intensity or no diffraction lines for thinner films. Wang et al. [41] investigated ZrN coatings at various temperatures. Columnar morphology with (220) grain orientation was achieved at 1300 ^{o}C, while equiaxed grain

structures were obtained at 1400 ºC. Another study used the RF magnetron sputtering approach to create Zr particulates with 5s nm grain size and (111) orientation at 400 ºC. However, as the temperature increased from room temperature to 400 ºC, the morphology smoothed out, and the grain size increased.
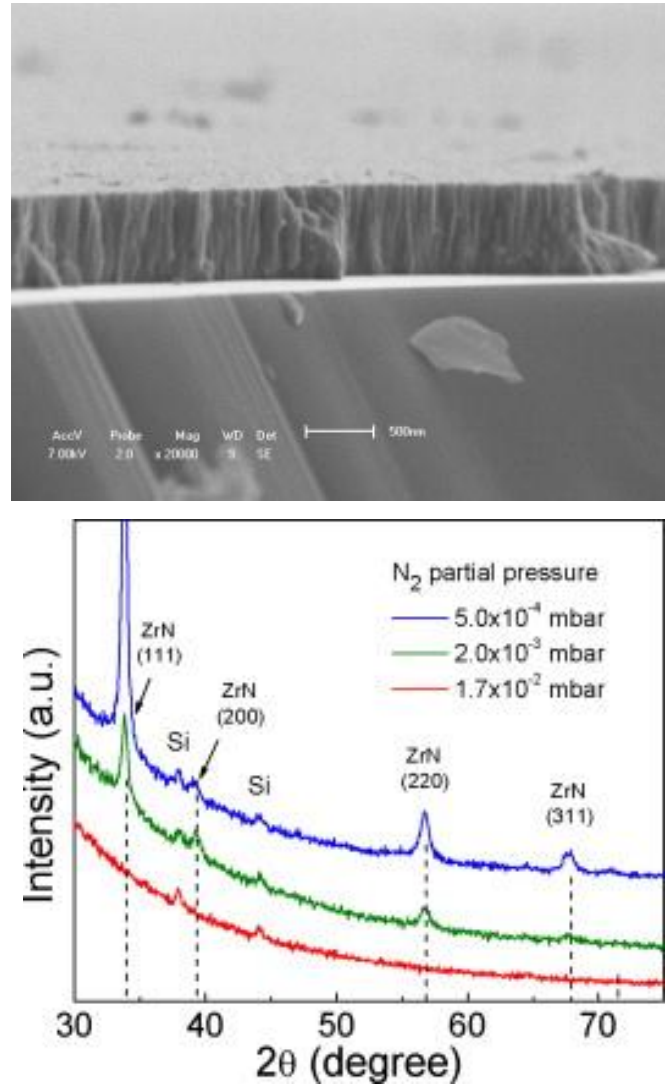
Figure 2.2: Cross-sectional SEM image of samples deposited with partial pressure of 1.0×10^{-3} mbar (top) XRD patterns for ZrN thin film at different N_2 partial pressures (bottom) [30].

Silva et al. [42] deposited ZrN coatings using DCMS at a different rate of N_2 under low ion bombardment, as shown in *Figure 2.3*. A porous columnar morphology has been seen at a modest N_2 flow rate, according to *Figure 2.3a*. Denser morphology and finer grains were formed when N_2 flow increased due to improved grain re-nucleation (*Figure 2.3b,c*). Tiny grains are the key feature of this structural type because grain expansion through coalescence is severely constrained due to the limited mobility of grain borders covered with high nitrogen flow.
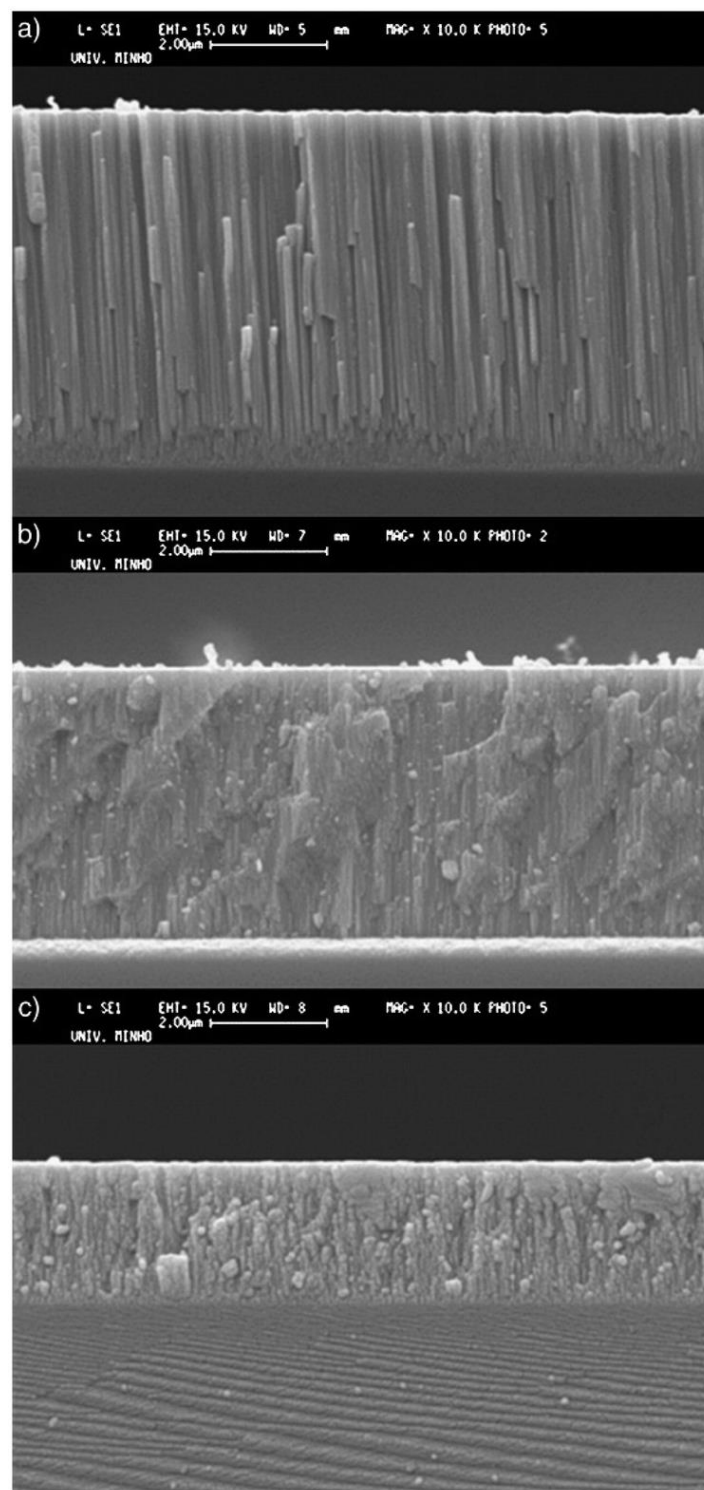
Figure 2.3: *(a) Cross-section of SEM coating deposited at different N₂ flows: (a) 2 sccm, (b) 6 sccm, and (c) 10 sccm [42].*

2.3.6.   Applications of Zr-nitride coatings against corrosion and oxidation resistance

ZrN coatings have been deposited to stop corrosion growth under maritime conditions. Budke et al. [43] have assessed the corrosion resistance of ZrN film on the substrates used in bathroom accessories. The result showed an improvement in the corrosion resistance of sanitary equipment when coated with ZrN. The coating resistance could be significantly improved by altering the sputtering parameters in the process. Investigation of corrosion resistance of ZrCN is studied by Gu et al. [44]. The authors stated that ZrCN hard coating deposited by arc plasma prevented the substrate corrosion resistance. The corrosion behaviour of ZrN on Ti-6Al-4V alloy was investigated using electrochemical techniques at different temperatures ($25^{o}C$, $55^{o}C$, and $70^{o}C$). It was tested that with increasing temperature, the defects of passive film on the surface increases. Meaning that the passive layer found less protective by increasing temperature. Moreover, the defective pits on the passive film as a function of temperature increases as shown in *Figure 2.4*, under same conditions of un-coated (*Figure 2.4a*) and coated (*Figure 2.4b*).
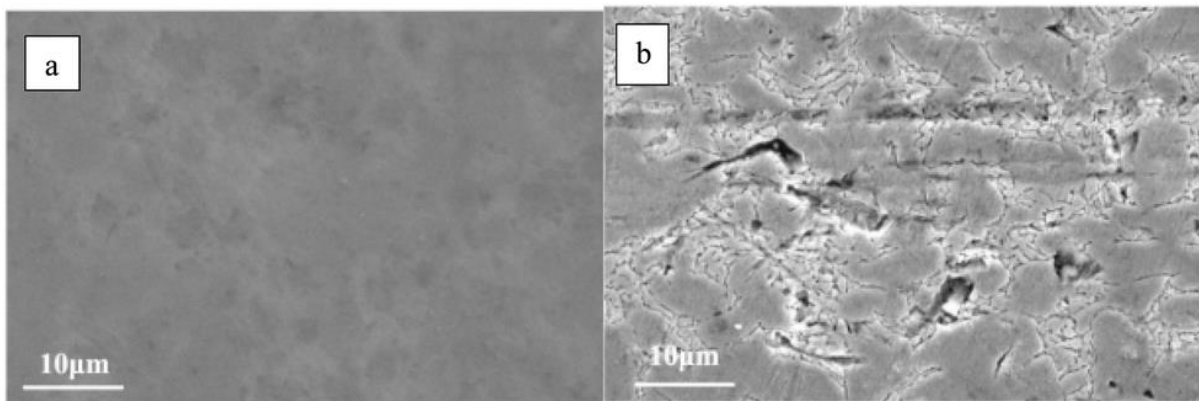
*Figure 2.4: : The corroded surface morphologies of (a) un-coated and (b) Zr coated Ti-6Al-4V after potentiodynamic polarization performed in 0.5 M H2SO4 solution [44].*

Ferreira et al. [45] investigated the corrosion resistance of ZrN and ZrSiN on magnetron sputtered AISI 430. It was discovered that the ZrSiN coating was more effective than ZrN coating in protecting steel against corrosion. The ZrN coated AISI steel showed localised corrosion due to presence tiny pores in the coating, but the ZrSiN coated steel prevented uniform corrosion. ZrN thin film deposited using DC reactive magnetron sputtering has been observed for corrosion behaviour in the biological medium [46]. Stable and long potential range deposition was studied in artificial saliva. The pitting potential increased as deposition temperature increased on the coated surface during the synthesis process. Considering 500 ^{o}C temperature, the pitting potential was observed as $E_{p} = 1.5$ V

vs SCE. As the process temperature enhanced, the corrosion behaviour declined because of thin-film (ZrN_xO_y and ZrO_2) formation on the top surface of the layer.

2.4. Deposition techniques

There are several deposition methods for producing coatings, such as cathodic arc deposition [47] [48], ion beam deposition [49], pulsed laser deposition [50], and chemical vapour deposition [51]. However, in a vacuum environment, these can be divided into two groups: (i) those involving thermal evaporation techniques, in which the material is heated in a vacuum until its vapour pressure exceeds the ambient pressure, and (ii) those involving ionic sputtering methods, in which high-energy ions strike a solid and knock off atoms from the surface.

2.4.1.   Magnetron sputtering deposition

Magnetron sputtering is a high-rate vacuum coating process used to deposit metals, alloys, and compounds onto various materials with very low thicknesses. It has significant benefits over other vacuum coating processes, leading to the development of several commercial applications spanning from microelectronics production to corrosion resistance. Magnetron sputtering is a type of physical vapour deposition that involves pushing materials from the source to the surface of the substrate. Particles are ejected from the source during sputtering (see *Figure 2.5*), but only a small area is ionised. Instead, the energized ions shoot in a straight line to impinge on the substrate, leading re-emission of deposited materials from the substrate's surface (i.e., re-sputtering) [52]. Their advantages allow a hard production coating using a wide range of deposition parameters to obtain films of various compositions, morphologies, and desired structural properties [53]. Nitride coatings are usually achieved in a mixed Ar-N_2 environment at low pressure (10^{-2} mbar). Compared to alternative coating processes, the rate of deposition and composition as a function of N_2 partial pressure and flow have been often tested, giving improved properties [54].
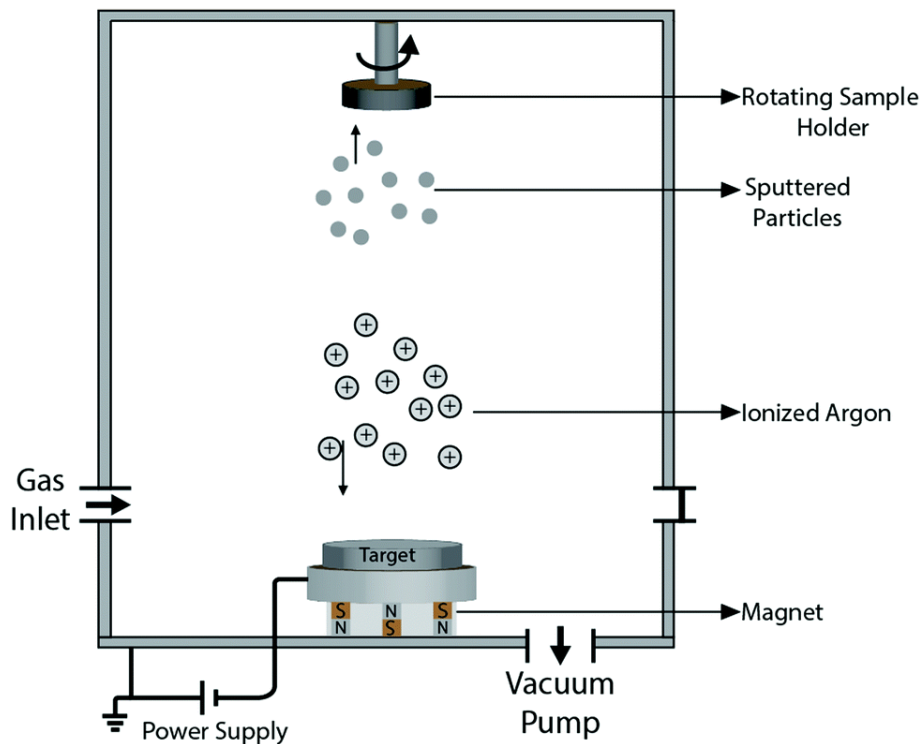
Figure 2.5: *Schematic display of a magnetron sputtering technique [52].*

Other vacuum coating processes like thermal evaporation and electron-beam evaporation, have been replaced by magnetron sputtering [52]. However, there are some drawbacks to these methods. Alloys and refractory metals create problems due to variances in alloy constituent vapour pressures and high melting temperatures (the need to run sources very hot, thereby affecting the coated articles). Furthermore, compounds might break into their chemical constituents due to the low evaporation pressures [55]. Magnetron sputtering, for example, overcomes these issues while still providing other benefits as follows:

- High film adhesion and deposition rates.
- Ease of sputtering and metal, alloy or compound.
- Extensive coverage of steps and minor details.
- Heat-sensitive substrates can be coated.
- High homogeneity and ease of automation over a vast surface area.

Despite of many advantages of magnetron sputtering, this technique has some limitations. Due to a decreased ($< 40\%$) usage rate, once the sputtering groove of magnetron sputtering penetrates the target, the entire target will be destroyed [11]. Furthermore, high-speed sputtering at low temperatures for strong magnetic materials is impossible because

practically all magnetic fluxes cannot pass through the magnetic target. Hence, is not possible to apply an external magnetic field near the target surface [31]. To circumvent these issues, a sophisticated and modified deposition process known as DOMS can be used.

2.4.2. Deep oscillation magnetron sputtering (DOMS)

DOMS is a new thin-film deposition method that has attracted the interest of both industry and academia [10]. DOMS is a PVD process in which power is applied to the target at a low frequency (10 kHz) and cycle (10%), resulting in pulse target power of many kW cm^{-2}. The degree of ionisation (plasma particles) in the magnetron sputtering technique is quite variable, resulting in a low total ion flux of the expanding film [56]. However, the practical realization of the DOMS process requires efficient and more advanced power than those used in conventional magnetron sputtering methods. The low average target power is essential to protect against the damage and overheating the cathode and the target. *Figure 2.6* depicts a schematic view of DOMS, a DC generator connected to the magnetron to load the capacitor bank of the pulsing unit. The charging voltage of the capacitor stored energy from several volts to kV and released in the pulse of defined frequency and width between the capacitor and the cathode. The high target current densities are accompanied during the pulse on time with electrical characteristics of the discharge, as demonstrated by magnetron sputtering operating in a dcMS mode. One of the advantages of this technique is that it can operate in an extensive range of power densities.
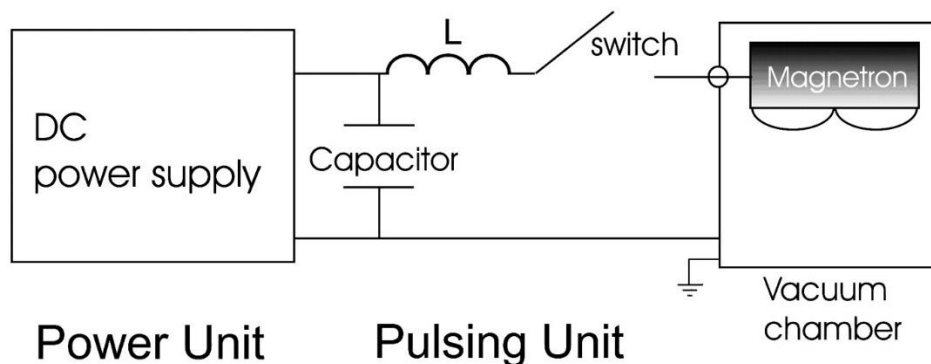

Figure 2.6: Basic architecture of a DOMS power supply. A DC generator charges the capacitor bank of the unit [10].

2.4.2.1. Growth of the thin films and morphology produced by DOMS

Changing the deposition parameters in DOMS allows for control of the energy delivered to the film‑forming species, allowing for manipulation of the film's characteristics [57]. Ionized species bombardment is one of the several methods utilised to deliver energy to the growing film [58]. Numerous investigations have revealed that the energy of the bombarding ions, their flux, type, and incidence angle all affect the plasma-film interface during film growth [59]. These factors control the efficiency of momentum transfer to the film atoms [60] and have been demonstrated to influence the film microstructure as well as mechanical, optical, and electrical properties [61]. Adjusting process parameters such as peak target current, pressure, deposition angle, and magnetic field intensity can change the amount and substance of these fluxes. Thornton et al. [62] reported a Structure Zone Diagram (SDZ) that describes the microstructure of thin film deposited by magnetron sputtering, considering both process pressure and temperature. However, this diagram does not account for the effect of additional ion bombardment when ion-assisted deposition (such as substrate biasing). Messier et al. incorporated this impact by proposing a modified diagram in which the pressure axis was substituted with an ions energy axis [63].

This diagram, in turn, ignores the atoms/ions ratio that reaches the substrate, the mass differential between ions and atoms that contributes to film formation, and the fact that ions can have a comprehensive energy distribution. Recently, Anders [64] proposed a new SDZ for HiPIMS modifications to the Thornton diagram:

- To obtain a generalised temperature axis, a term was added to the homologous temperature axis that accounts for the effect of the potential energy of the particles arriving at the substrate.
- The linear pressure axis has been replaced by a normalised logarithmic energy axis that accounts for the displacement and heating effects caused by the bombardment particles' kinetic energy.
- A Z-axis was defined as the net film thickness to dictate the film reduction due to the film sputtering and densification.
- *Figure 2.7* shows SDZ reported by Anders, and these zones are similar to those proposed by Thornton.
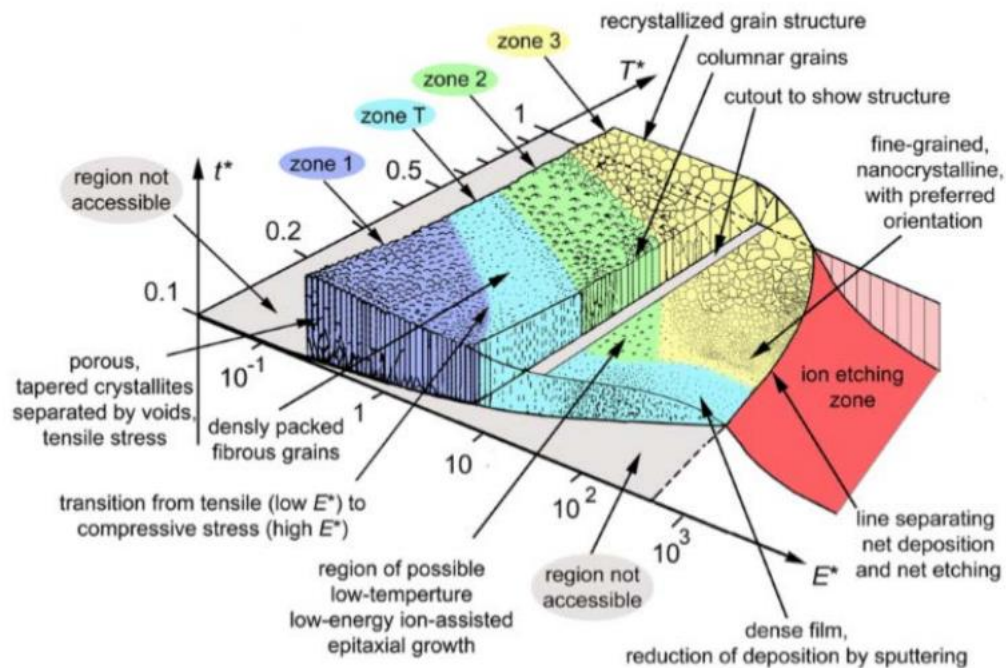
Figure 2.7: *Structure zone diagram applicable to energy zone [64].*

A case of the aforementioned is presented by Elmkhah et al. [65] deposited TiN coatings on carbon steel and Si wafers by DOMS and DCMS techniques. The SEM micrographs, comprising cross-section and top views, are shown in *Figure 2.8*. TiN coatings for DOMS appear to be highly smooth and free of macro-droplets, which are critical for coating protection. Although both coatings appear to have a columnar growth topology, the DOMS coating appears finer than the DCMS coating. The growth structure is well recognised to significantly impact the mechanical and electrochemical performance of these coatings [13]. Another study [66] investigated the behaviour of DOMS sputtering on a metal surface in an O_2/Ar mixed atmosphere. The results reveal that a high waveform current generates during DOMS pulses and that deposition behaviour exhibits optically transparent coatings throughout a wide range of oxygen fluxes. Ghailane et al. [67] reported the influence of magnetic field strength and hardness of TiN coatings deposited by DOMS and DCMS. DOMS resulted in defect-free and high-density barrier coatings against wear and corrosion. Furthermore, increasing the magnetic field strength on the deposition rate increased the hardness of nitride coatings deposited by DOMS over DCMS. Overall, DOMS-deposited films had good structural and mechanical properties.
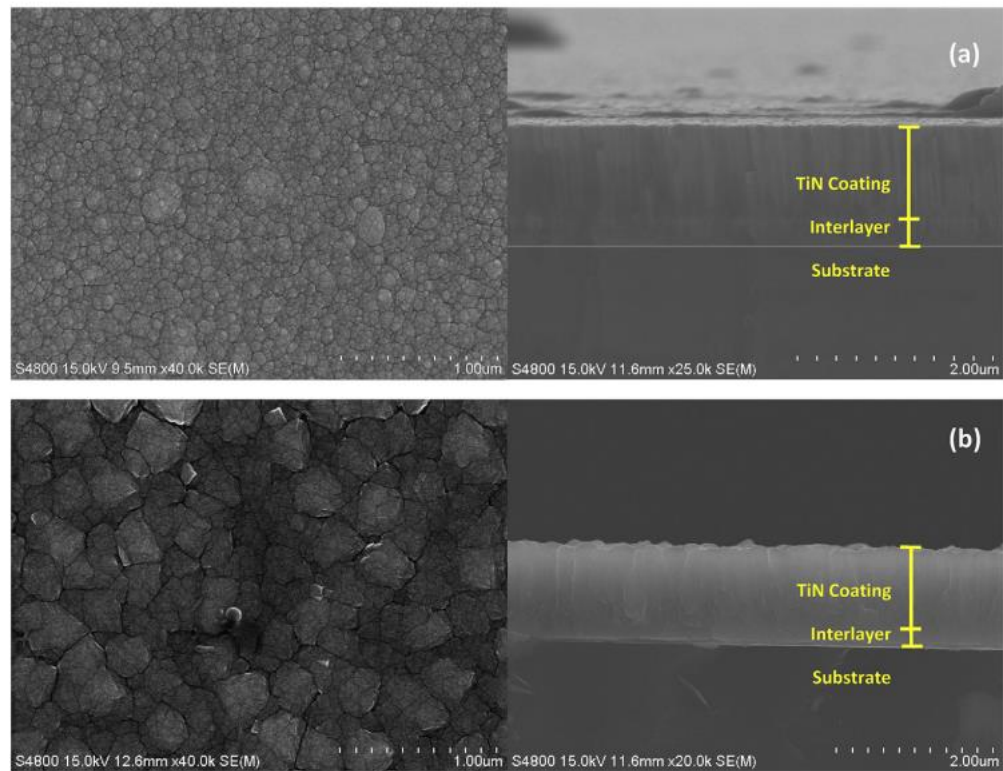
Figure 2.8: *SEM micrographs of the TiN nanostructured coatings (both cross-section and top view) deposited by (a) DOMS and (b) DCMS techniques [67].*

CHAPTER 3

3. METHODOLOGY AND CHARACTERIZATION

This chapter presents the experimental aspects carried out during the thesis. The first section is related to the materials preparation and various protocols to obtain coatings. Furthermore, the characterization techniques practised in the research are discussed in detail.

3.1. Materials

The zirconium nitride (ZrN) depositions were performed on commercial 316 L stainless steel (SS) and (100) silicon substrates of 2 cm^2 area and 0.5 mm thickness.

3.1.1. Sample preparation

SS samples were polished before coatings to avoid any aspect related to the topography of the substrate. Next, a series of emery papers (i.e., 600, 800 and 1200) were utilised to remove any scratch on the surface, followed by polishing the samples using velvet cloth and diamond suspension (6 μm and 3 μm). Lastly, the samples were cleaned with acetone and ethanol in an ultrasonic bath for 15 minutes. On the other hand, silicon samples were cleaned only in an ultrasonic bath with the sequence of acetone and ethanol for 15 minutes each. The samples were then glued onto a rotating sample holder (made of aluminium) with electrically conductive silver glue. The sample holder revolves at a speed of ~24 RPM around the central axis inside the deposition chamber.

3.2. Deposition chamber

The depositions of this work were performed using a modified commercial deposition chamber from HARTEC (see *Figure 3.1a*) made of high-grade SS. The chamber contains two cathodes (fixed and movable) placed inside the adjacent walls. A shutter inside

the chamber functions as a barrier between the target and the substrates, allowing the target and the substrates to be cleaned before the depositions. Only the fixed cathode was employed with a pure Zr target (150 x 150 mm^2) for the depositions. The distance between the target and the substrates is 8 cm. A mechanical and turbomolecular pumps system was used to achieve a base pressure of less than 9 x 10^{-4} Pa before all depositions. The coatings were deposited in DOMS mode using a Cyprium^{TM} III plasma generator (Zpulser Inc.) as shown in *Figure 3.1b* and by DCMS using Hüttinger PFG-7500 DC power supply.
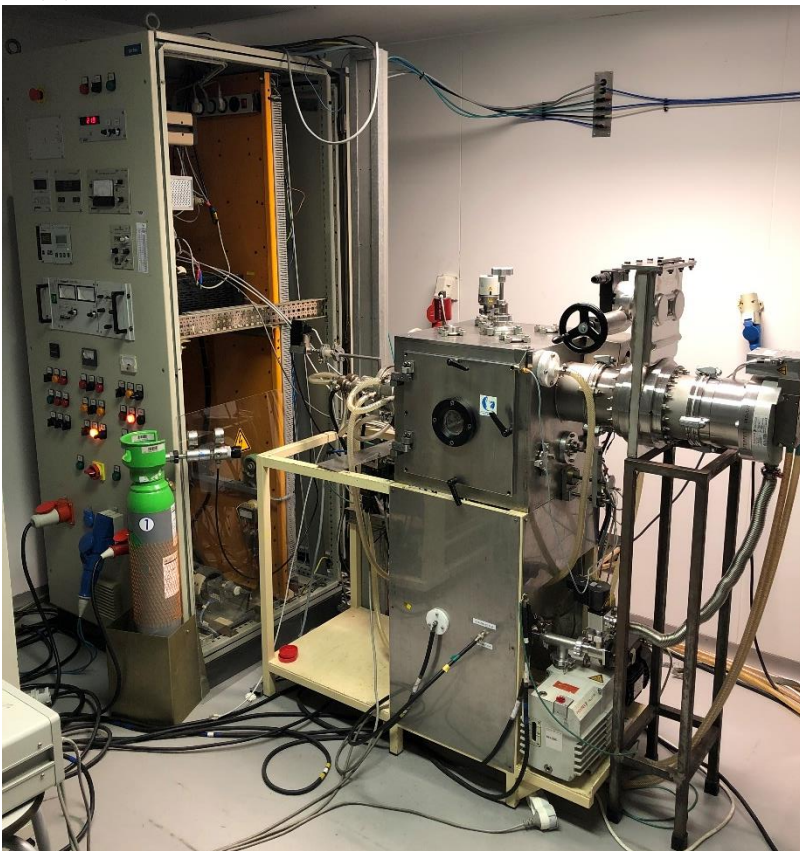
(a)   **(b)**

Figure 3.1: *(a) Deposition chamber (b) DOMS power supply used for this work.*

3.2.1. ZrN deposition process

A series of depositions were performed on substrates in the DOMS mode of the power supply and the conventional sputtering process in a reactive atmosphere (Ar + N_2) to obtain the ZrN films. To perform a final cleaning on the surface of substrates, a plasma etching procedure for 1 hour was performed prior to all depositions using a pulsed DC power source (-350 V, 120 kHz frequency and 1616 ns pulse width) connected to the substrate holder in Ar atmosphere at 0.3 Pa working pressure. At the same time, the Zr target was cleaned, inducing a slight plasma (250 W) with the DC power supply. A shutter was positioned between the substrate and target to avoid substrate contamination.

Two working pressures (0.4 and 0.7 Pa) were defined. At first, the pure Zr interlayer was performed to achieve an improved ZrN coating to the substrates. In DCMS films, -50 V bias voltages and 1200 W of target power were kept constants for all coatings. In DOMS depositions, the applied pulses were adjusted to 36 μs period and the duty cycle was set to 12/24 μs as on- and off-time (t_{ON} and t_{OFF} respectively). Also, the pulse duration was constant (1000 μs) and the substrate holder was not connected to any equipment (floating state). Besides, the input voltages for the internal DC power source of the Cyprium plasma generator varied depending on the optimization with the N_2 flow and the working pressure. For the DCMS coatings, 45 and 50 % N_2 flow were selected for 0.4 and 0.7 Pa working pressure, respectively to obtain coatings close to the stoichiometric conditions. *Table 3.1a* and *Table 3.1b* show the additional parameters employed for DOMS and DCMS coatings, respectively.

Table 3.1a: *Deposition conditions of the ZrN film coated by DOMS at different parameters*

Sample	Label	Volt(V)/N_2 flow(%)/pressure (Pa)	Ar flow (%)	V_p (V)	I_p (A)	P_p (kW)	F (Hz)	Targeted volt. (V)
ZrN-DOMS	A	300/30/0.4	17.89	1066	126.14	134	131	346
ZrN-DOMS	B	300/40/0.4	16.11	1063	109.00	115	132	325
ZrN-DOMS	C	300/60/0.4	12.61	1060	94.50	100	132	327
ZrN-DOMS	D	300/80/0.4	9.49	1053	93.30	98	138	350
ZrN-DOMS	E	350/80/0.4	9.18	1232	151.56	186	78	352
ZrN-DOMS	F	250/50/0.7	14.83	866	64.33	55	194	329

Table 3.1b: *Deposition conditions of the ZrN film coated by DCMS at different parameters*

Sample	Label	N₂flow(%)/pressure (Pa)	Ar flow (%)	V (V)	I (A)	P (W)	Bias		Targeted volt. (V)
							V(V)	I (A)	
ZrN-DCMS-0.4-45	G	45/0.4	17.30	365.5	3.37	1230	-50	1.20	317
ZrN-DCMS-0.7-50	H	50/0.7	16.05	358.5	3.43	1231	-50	1.39	325

3.3. Characterization methods

3.3.1. Scanning Electron Microscopy (SEM)

The morphology of the samples was taken using a Hitachi SU3800 scanning electron microscope, which uses the reflected or knocked-off electrons near the surface region to create an image. The standard magnification used for evaluation was between 10–40 kX and the power of the electron beam used for SEM images was 10 kV.

3.3.2. Energy Dispersive X-ray Spectroscopy (EDS) analysis with SEM

EDS analysed the chemical composition of ZrN films. The same SEM equipment is used for EDS analysis with an Oxford instrument module that permits identifying and quantifying the elemental composition of all coatings. For all measurements, the beam energy of 15 kV was employed to obtain the excitation of the required elements.

3.3.3. X-ray Diffraction (XRD) measurements

XRD is a high precision analysis tool that provides essential information related to phase transformation and structural characteristics of the samples. In this work, X'Pert PRO model: PANalytical XRD (PANXRD) instrument was used to obtain XRD patterns of each

film. X'Pert Pro MPD diffractometer in conventional (θ–2θ) mode was setup in the range of $2\theta = 30$–80° with CuKα source radiation (45 kV, 40 mA and $\lambda = 1.5406$ nm).

3.3.4. Electrochemical corrosion testing

A three-cell electrode system was used to study the corrosion behaviour of coated (ZrN) and non-coated (SS) samples. Concerning electrodes, the saturated (with KCl) calomel electrode (SCE) was used as a reference, a pure Pt sheet as a counter electrode and the substrate was the working electrode. The Electrochemical Impedance Spectroscopy (EIS) and potentiodynamic dynamic curves were measured in artificial seawater (3.5% NaCl solution) using GAMRY potentiostat. The parameters applied for the EIS test are given in *Table 3.2a*. To simulate the experimental results for EIS curve fitting and obtaining the electrical equivalent circuit, GAMRY Echem Analyst software was used. On the other hand, potentiostat dynamic measurements were performed by DC mode to analyse the corrosion rate of the films. The parameters of potentiostat are given in *Table 3.2b*. The corrosion rates were calculated by eq. (1), whereas polarization resistance was measured using eq. (2).

$$\text{Corrosion rate } (CR) = K_{corr} \left(\frac{i_{corr}}{\rho} \right) EW \; (mm/\text{yr}) - (1)$$

$$i_{corr} = \left(\frac{I_{corr}}{A} \right) \; (\mu m/cm^2), \; A = area \; (cm^2), \; I_{corr} = \frac{B}{R_p}, \; B = \frac{\beta_a \cdot \beta_c}{2.303(\beta_a + \beta_c)}, \; K_{corr} = 3.27 \times 10^{-3}$$

$$\left(\frac{mm \; g}{\mu A cm \; y} \right), \; \rho = \text{density}, \; EW \text{ (equivalent wt. of coatings)} = \frac{A_{wt}}{n}, \; A_{wt} = \text{atomic weight}, \; n = no.$$

of electrons

$$I_{corr} = \frac{1}{R_p} + \left(\frac{\beta_a \cdot \beta_c}{2.303(\beta_a + \beta_c)} \right) - (2)$$

*Table 3.2a: Parameters used for EIS corrosion test*

Test identifier	Initial freq. (Hz)	Final freq. (Hz)	Decade	AC volt (mV)	Area (cm^2)	Time (s)
Potentiostatic EIS	100000	0.01	10	10	0.35	3600

Table 3.2b: *Parameters used for potentiostat dynamic measurements*

Test identifier	Initial E (V)	Final E (V)	Scan rate (mV/s)	Area (cm^2)	Time (s)
Potentiostatic dynamic polarization	-0.5	1.5	1	0.35	3600

The cell (see *Figure 3.2*) consisted of a 150-200 mL acrylic beaker filled with approx. 120 mL with 3.5% NaCl solution (used as an electrolyte) for all experiments. The sample was fitted between the hollow space (0.35 cm^2 exposed area) contacted with the electrolyte. All tests were run at room temperature of (25 ^{o}C) and static pressure mode with naturally aerated.
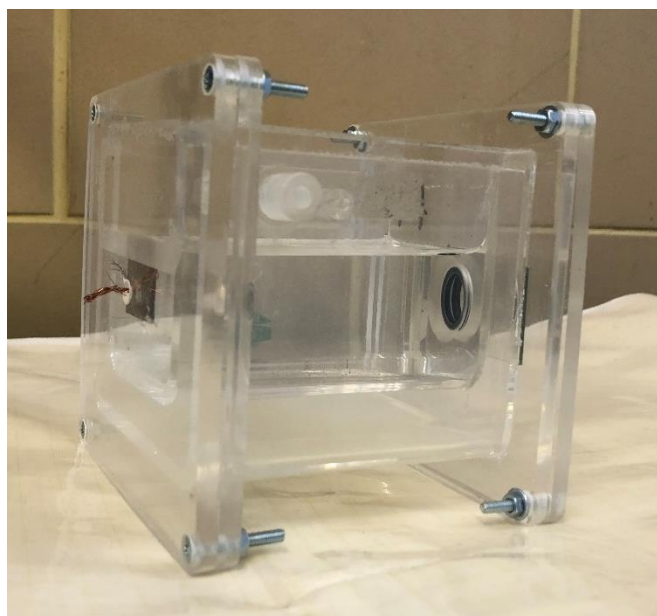
Figure 3.2: Cell used for corrosion tests

3.3.5.   Tribological characterization

The wear resistance or tribological tests were carried out using the pin-on-disc instrument in both dry (25 ^{o}C) and wet conditions (in this way, free corrosion could lead to mechanical surface interactions in the tribological contact). The tribo-corrosion phenomenon is very important to be measured in seawater since the wear rate (due to severe corrosion attack) is higher than open atmosphere. The samples were immersed in 3.5 wt.% NaCl solution (used for all corrosion tests). An alumina ball with a diameter of 6 mm was used. During the sliding/friction testing, a load cell was used to determine the friction coefficient,

and the findings were then transferred to a computer for further analysis. All tests were conducted with a standard load of 2 N and 200 m distance [32]. Other experimental conditions are shown in *Table 3.3*.

Table 3.3: *Experimental conditions for pin-on-disc test*

Load (N)	Velocity (mm/s)	Sliding distance (m)	RPM	Time (s)	Ball diameter (mm)
2	50	200	79.6	3967	6

Wear profiles from various regions of the wear track were collected using 2D profilometer. The profilometer results were plotted using OriginPro 2020 software to calculate the area of delaminated coatings and materials from the wear tracks. Following that, eq. (3) was applied to obtain wear rate:

$$\text{wear rate } (k) \ (mm^3/N.m) = \frac{vol. of \ wear \ track \ (mm^3)}{load \ (N) \ x \ distance \ (m)} = \frac{Area \ (A) \ x \ length \ (l)}{Load \ (L) \ x \ distance \ (m)} - (3)$$

where, *A* is the area of the wear track, *k* is specific wear rate, *N* is applied load, *m* is the sliding distance.

CHAPTER 4

4. RESULTS AND DISCUSSION

This chapter discusses in detail about the outcomes of all deposited coatings. The comprehensive discussion on electrochemical tests, i.e., EIS, potentiodynamic polarization curves and tribological tests, are elaborated.

4.1. SEM morphology and EDS analysis of ZrN coatings

The surface morphology (top view) and cross-section of ZrN coatings deposited by DOMS and DCMS are shown in *Figure 4.1*. The coatings deposited by DOMS (A–F) are very smooth and free of macro-cracks which are critical and detrimental to the effectiveness of these coatings. Compared to the DCMS coatings, the DOMS coatings appear finer and denser. The compact morphology of the substrates has been observed from the top view (see *Figure 4.1* (A2–F2)) of the ZrN films deposited by DOMS. It should be noted that increasing voltages ~300 V and N_2-flow play an equivalent role in changing the morphology of the thin film. Increasing N_2-flow (from 30–80%) on the samples (A–E) gradually increased the dense morphology.

On the other hand, ZrN coatings deposited by DCMS display a compact morphology (*Figure 4.1*G-H), however it is possible to distinguish the columnar extending from the surface of the substrates to the top. Although the power was kept constant at ~1230 W for both samples (G, H), the N_2-flow changed 45 to 50%, respectively. Looking at the top-view micrographs (*Figure 4.1* G2–H2), the columns are domed, and the coatings resemble a cauliflower-type morphology with non-homogeneity.
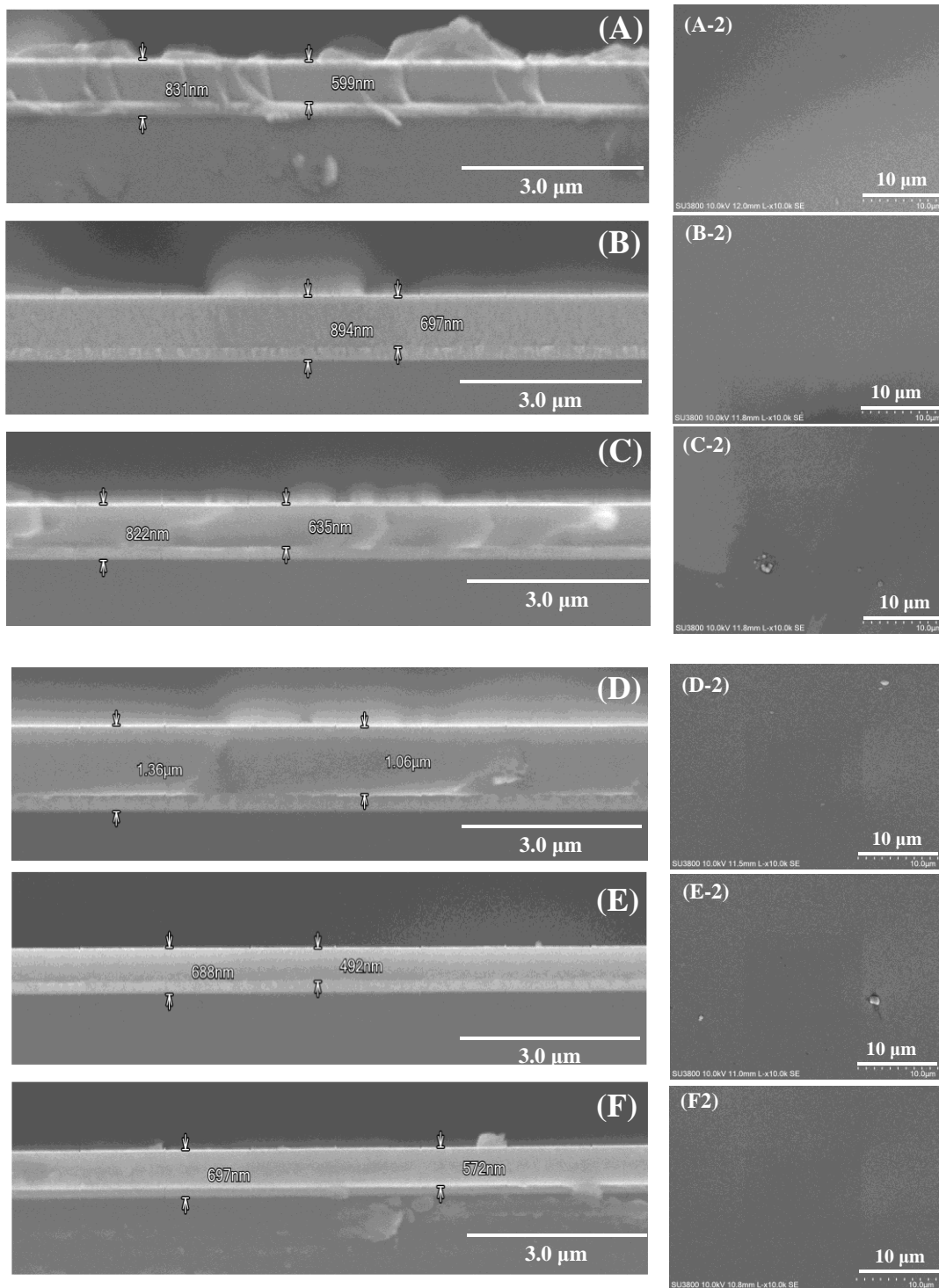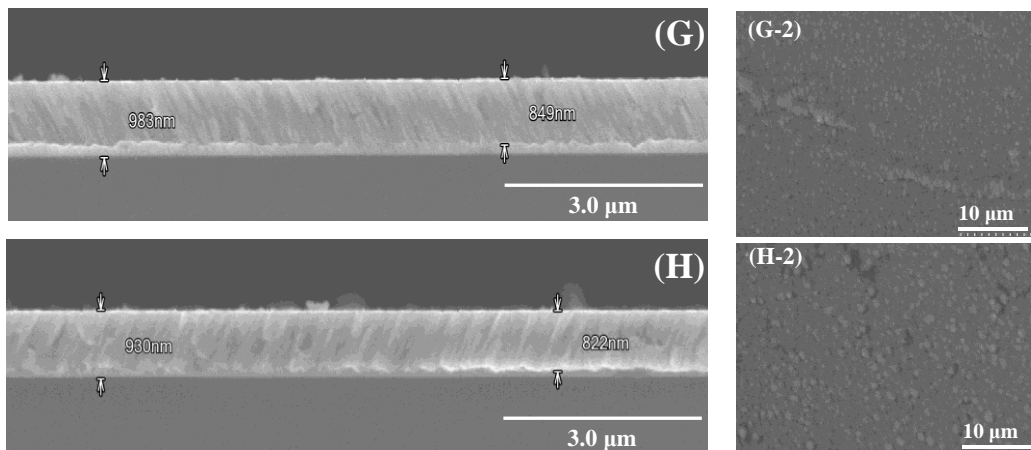
Figure 4.1: *SEM images of ZrN films deposited via (A-F) DOMS and (G,H) DCMS. Cross-section (left) and top-view (right)*

The thicknesses of all samples are presented in *Figure 4.2*. Clearly, no significant difference in thickness has been observed on samples (A–C), the ZrN coating's thickness was recorded between 820–895 nm. The cross-section of the samples (E–F) on which thickness of the ZrN layer was achieved as 492 and 572 nm, respectively. Nevertheless, a vast difference among all these samples can be seen on sample (D) in which the ZrN coating was achieved with the highest thickness (1060 nm) due to involvement of highest N_2 flow (80%). On the other hand, the coating thickness of 930 and 983 nm were attained on the samples G and H, respectively. A similar trend was examined for pure Zr film on all substrates but with lower thickness because the deposition time for Zr film was optimized in order to avoid high layer.
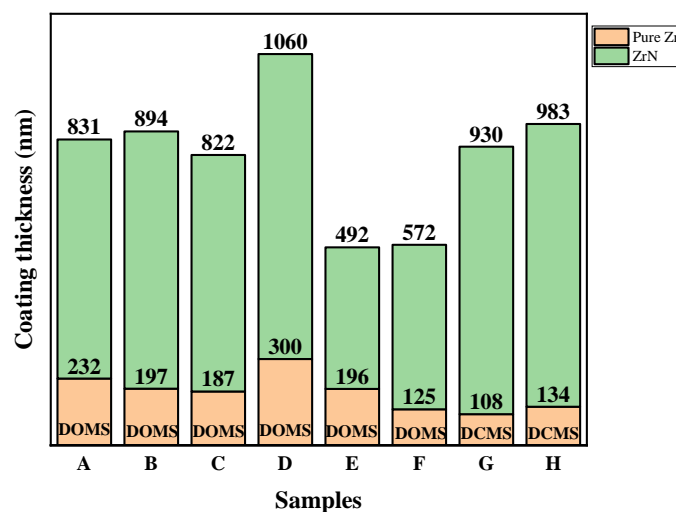

Figure 4.2: *Coating thickness plot of ZrN films deposited via (A–F) DOMS and (G-H) DCMS*

Figure 4.3 shows the EDS analysis of the ZrN coatings. The elemental composition indicates the presence of only Zr and N on all samples (A–H) except (E–F), on which a small quantity (7.65 and 3.65 at.%, respectively) of Si in addition to Zr and N was analysed. The appearance of Si is mainly due to low film thickness (see *Figure 4.2*) on both samples. It should be worth noting that the atomic percentage of N_2 on all samples (coated via DCMS and DOMS) is ~50%.
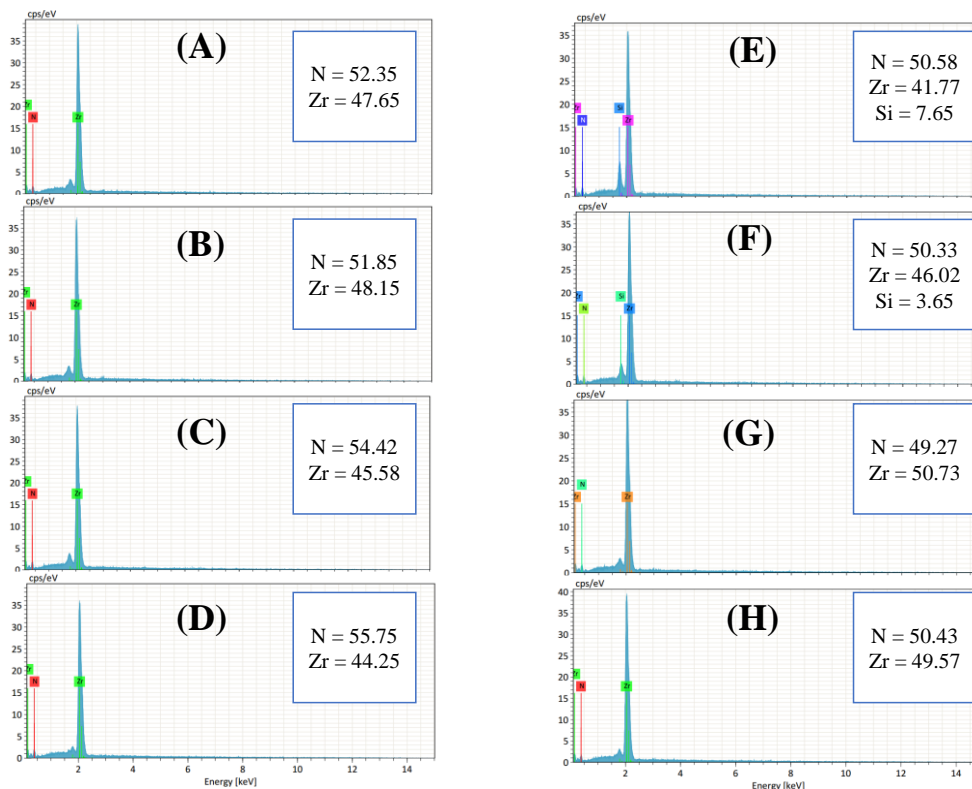

Figure 4.3: EDS analysis of the ZrN films deposited via (A-F) DOMS and (G-H) DCMS

4.2. XRD results of ZrN coatings

Figure 4.4 shows the XRD patterns of ZrN nanostructured coatings. According to ICDD reference codes: 031-1493 and 005-0665, all the diffraction patterns belong to typical ZrN (Na-Cl type structure) and Zr (hcp) polycrystalline structures, respectively. The peak at $2\theta = 33.9^{\circ}$ corresponds to the (111) plane of ZrN [68]. For this phase, the plane was preferred oriented considering all diffractograms (see *Figure 4.4a,b*). It can be observed that the intensity of the ZrN peak on sample (A) is not fully revealed, possibly due to low N_2-flow (30%) [69]. The peaks originated at $2\theta = 34.8^{\circ}$, the most intense diffraction peak belonging to Zr. According to Ye et al. [69] the peak originates at the (311) plane and is also related to

ZrN. The peak intensity at the (002) plane decreased by increasing peak power and lowering N_2-flow in the case of DOMS. Other peaks at (100) and (200) planes in figure 4.4a and (100), (101) and (200) planes in figure 4.4b also correspond to Zr. Although the working pressure (0.4 and 0.7 Pa) and N_2-flow (45 and 50%) were different for film deposition, however, no significant variation in peak positions was observed for DCMS coatings (see figure 4.4b). The peak that appeared at $2\theta \sim 70^o$ is related to the Si substrate.
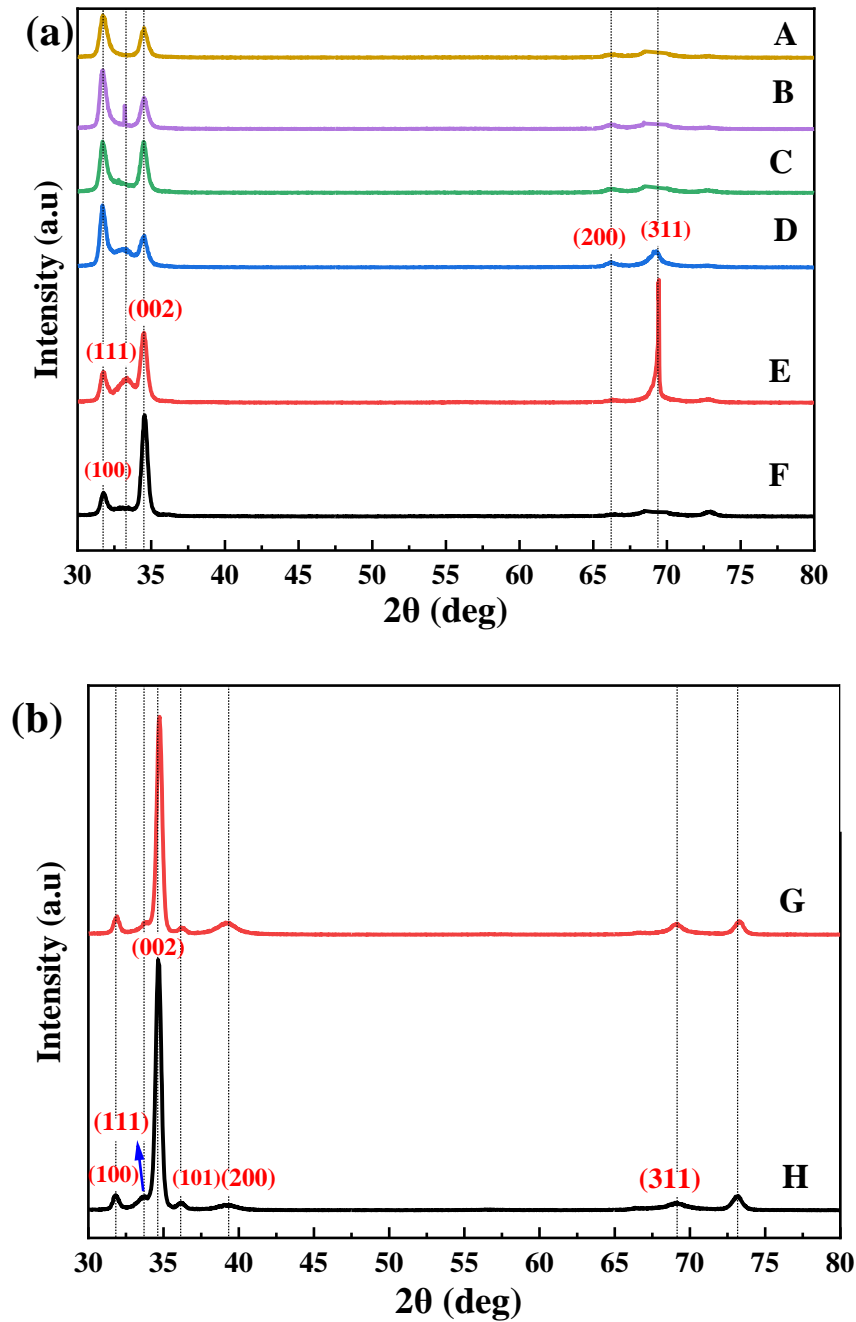

Figure 4.4: *XRD patterns of ZrN film deposited via (a) DOMS and (b) DCMS*

4.3. Electrochemical results

4.3.1.   EIS measurements

EIS of each sample was measured at time-lapse of 0 h, 24 h and 48 h in 3.5% w/w NaCl solution. An equivalent electrical circuit (EEC) (see *Figure 4.5*) was constructed to fit experimental data and perform a quantitative analysis. The R_{sol} is the resistance of 3.5% NaCl solution, the constant phase element (CPE_{coat}) is the coating capacitance constant, and R_p is the polarisation resistance. The present EEC has been widely adopted in the previous literature of ZrN corrosion studies [70, 71].
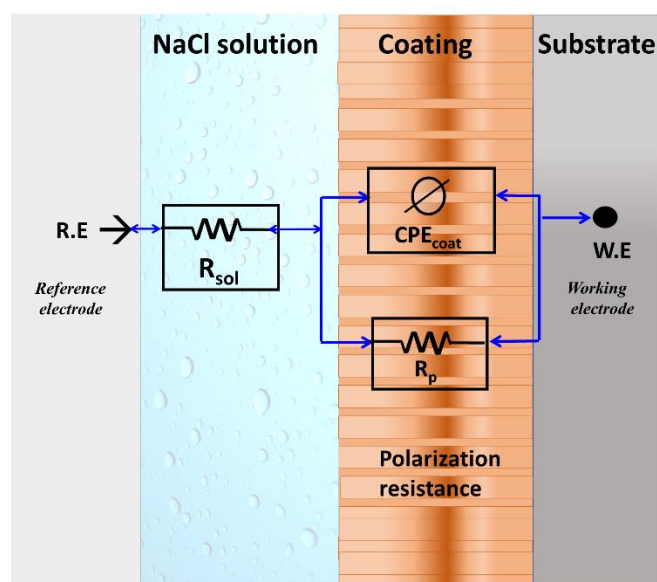

Figure 4.5: Equivalent electrical circuit for EIS plots. Adopted from GAMRY Echem Analyst software.

Figure 4.6 shows the Nyquist plots of DOMS and DCMS coatings compared with the uncoated substrate. *Table 4.1* illustrates the EEC fitted parameters of coated and uncoated SS. The sample's corrosion properties can be easily assessed by comparing the semi-circle of the loops in the Nyquist plots. Meaning that the larger capacitive loop controlled the corrosion in the test by a charge transfer process due to the protective film (Zr-N) on the substrate [72]. *Figure 4.6*A represents a direct comparison of all coated samples with the uncoated substrate at 0 h. It can be observed that the Z_{real} of DOMS coatings increased significantly – giving higher impedance (R_p) values in comparison with DCMS coatings and uncoated samples (see *Table 4.1*). A similar trend has been revealed for 24 h immersion time.

Interestingly, the impedance behaviour of DCMS-coated samples (G and H) was found lesser than the uncoated substrate. DCMS coatings were performed at low N_2 flow (45% and 50% for sample G and H, respectively), moreover, these coatings found as cauliflower/columnar morphology on the samples (see *Figure 4.1*). Looking at *Figure 4.6*C, the impedance of samples rises to the high values at 48 h of the test. The best results were obtained on DOMS-coated samples, specifically sample D (300V, 80% N_2 flow @ 0.4 Pa working pressure), which proposed the highest impedance behaviour among all samples. On the other hand, the uncoated and DCMS samples (G and H) exhibited the lowest impedance values at 48 h of exposure time (see *Figure 4.6*C and *Table 4.1*). The surface of DCMS coatings may have some surface defects, which could directly contact the electrolyte (saline solution), resulting in less corrosion resistance [65]. Clearly, owing to the more active anti-corrosion capability, sample D has shown higher impedance due to the dense ZrN (ceramics nature [73]) films.
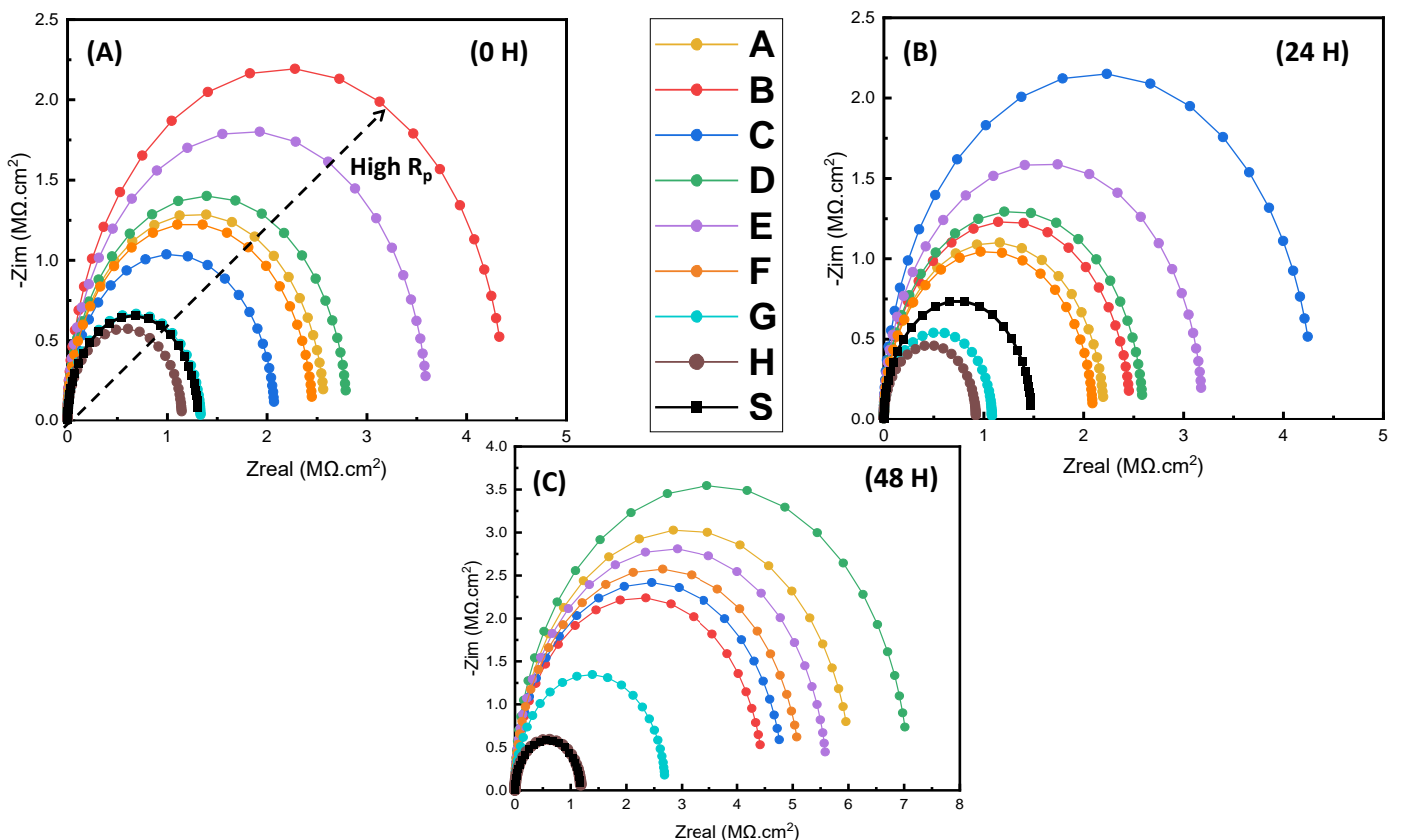

Figure 4.6: EIS results: *Nyquist plots of DOMS-ZrN and DCMS-ZrN coatings (A) 0 H (B) 24 H (C) 48 H*

Table 4.1: EIS fitting parameters of DOMS and DCMS coatings obtained by employing equivalent electric circuit.

Samples with coated conditions	R_{sol} ($\Omega*cm^2$)	R_p ($M.\Omega*cm^2$)	CPE_{coat} ($\mu S*/\alpha*cm^2$)	α
A-DOMS	287.86 ± 1.3	7.58 ± 0.62	5.84 ± 0.55	0.89 ± 0.03
B-DOMS	288.87 ± 1.9	5.76 ± 0.41	6.07 ± 0.41	0.89 ± 0.02
C-DOMS	288.33 ± 2.8	7.76 ± 0. 61	6.04 ± 0.60	0.88 ± 0.02
D-DOMS	369.03 ± 3.3	8.21 ± 0.58	5.09 ± 0.52	0.89 ± 0.02
E-DOMS	306.03 ± 2.1	6.07 ± 0.68	4.17 ± 0.66	0.88 ± 0.01
F-DOMS	287.83 ± 2.3	6.71 ± 0.56	5.41 ± 0.51	0.85 ± 0.02
G-DCMS	275.63 ± 3.1	3.27 ± 0.52	6.04 ± 0.48	0.85 ± 0.03
H-DCMS	252.46 ± 1.8	2.82 ± 0.21	8.91 ± 0.62	0.87 ± 0.01
S-uncoated	296.30 ± 1.5	2.59 ± 0.34	3.43 ± 0.79	0.84 ± 0.03

Results obtained by Bode plots have been shown in *Figure 4.7*. Coated samples have identified good barrier properties with a marked capacitive behaviour evident in the intermediate to higher frequency ranges as a function of time [70]. A relatable difference between Bode plots on coated and non-coated samples (see *Figure 4.7*A-S) were revealed to be associated with the nature of films. From *Figure 4.7*S, the uncoated sample exhibits a lower phase magnitude value (indicated by black dotted lines) compared to DOMS-coated samples at low frequency range. Over a broad frequency range, the phase angle values for DOMS-ZrN coatings (see *Figure 4.7* A–F) remain very near to -77°, while the phase angle values for DCMS-ZrN coatings (see *Figure 4.7* G and H) remain very close to -65°. It is stated that phase angles do not undergo significant changes (low values) on DOMS samples, suggesting less degradation of films as a time function. Cubillos et al. [74] reported that a phase angle close to 80° indicates a capacitive behaviour with good dielectric properties (more resistance), which is in good agreement with the findings of DOMS coatings in this research. It has been investigated that the coatings obtained by DOMS exhibited higher impedance due to the dense morphology of films incorporated with higher N_2 atoms to form ZrN at optimum pressure of 0.4 Pa. However, the impedance of DCMS-coated samples was recorded as lower, i.e., unable to achieve the dense and compact film of ZrN.
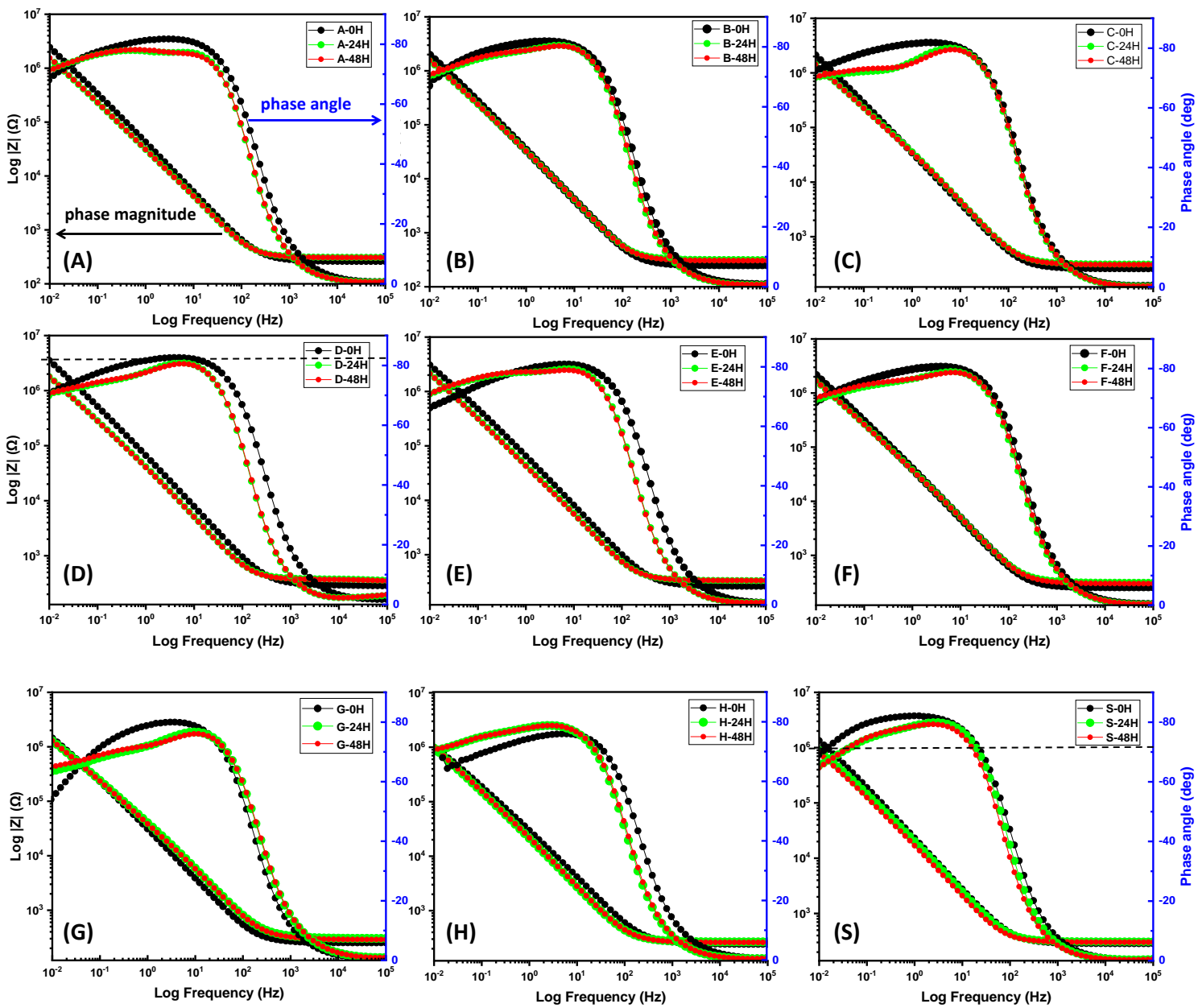
Figure 4.7: *EIS results: (A–F) Bode plots of DOMS- and (G,H) DCMS-ZrN coatings (S) uncoated substrate as a function of time (0, 24 and 48 H)*

4.3.2.   Potentiodynamic polarization measurements

Potentiodynamic polarization curves were measured in 3.5% NaCl solution to evaluate the corrosion rate, corrosion potential (E_{corr}) and corrosion current density (I_{corr}) of the coatings. *Figure 4.8* illustrates the polarization curves of ZrN coatings carried out by DOMS and DCMS as a function of time. The coated samples were compared with uncoated SS substrate (denoted by S in all plots) for 0 h to determine the comparison of corrosion behaviour. *Table 4.2* summarizes the values of I_{corr} and corrosion rate of ZrN coatings from the potentiodynamic/Tafel plots. The corrosion rates were calculated using eq. (1) by adjusting the equivalent weight and density of material according to the sample composition studied by EDS measurements (see *Figure 4.3*). I_{corr} is the critical parameter in the potentiodynamic polarization curves to evaluate the corrosion resistance of samples (lower the I_{corr} means better the corrosion resistance). *Figure 4.8*A.1,2 (samples obtained at 0.4 Pa and 0.7 Pa working pressure, respectively) show a direct comparison of all coated samples at 0 h of immersion time. E_{corr} values were found close to each other with minor changes (see *Table 4.2*). However, a substantial variation of I_{corr} values can be seen for the coated samples (compared to the un-coated sample). DOMS-coated samples revealed significantly lower I_{corr} and corrosion rates compared to DCMS-coatings. Among all DOMS-coating conditions, sample D (300 V, 80% N_2 @ 0.4 Pa) was considered a promising material, and sample F (250 V, 50% N_2 @ 0.7 Pa) was reflected as the worst coated sample.

Samples D, F, G, and H (of different coated conditions) were selected to conduct polarisation tests to assess the corrosion resistance over a long immersion period. *Figure 4.8*B-E displays the Tafel curves of specimens exposed at different durations (0, 24, 48 and 72 h of exposure time). Sample D has shown that the dense ZrN film hinders corrosion reaction. However, the film could not protect the surface of samples F, G and H as a function of time. The results suggest that DOMS coatings of highest N_2 flow (80%) with low working pressure ~0.4 Pa are more reliable and exhibit good corrosion protection through their long soaking period in 3.5% NaCl solution due to the dense (see *Figure 4.1*) and homogenous morphologies [70].
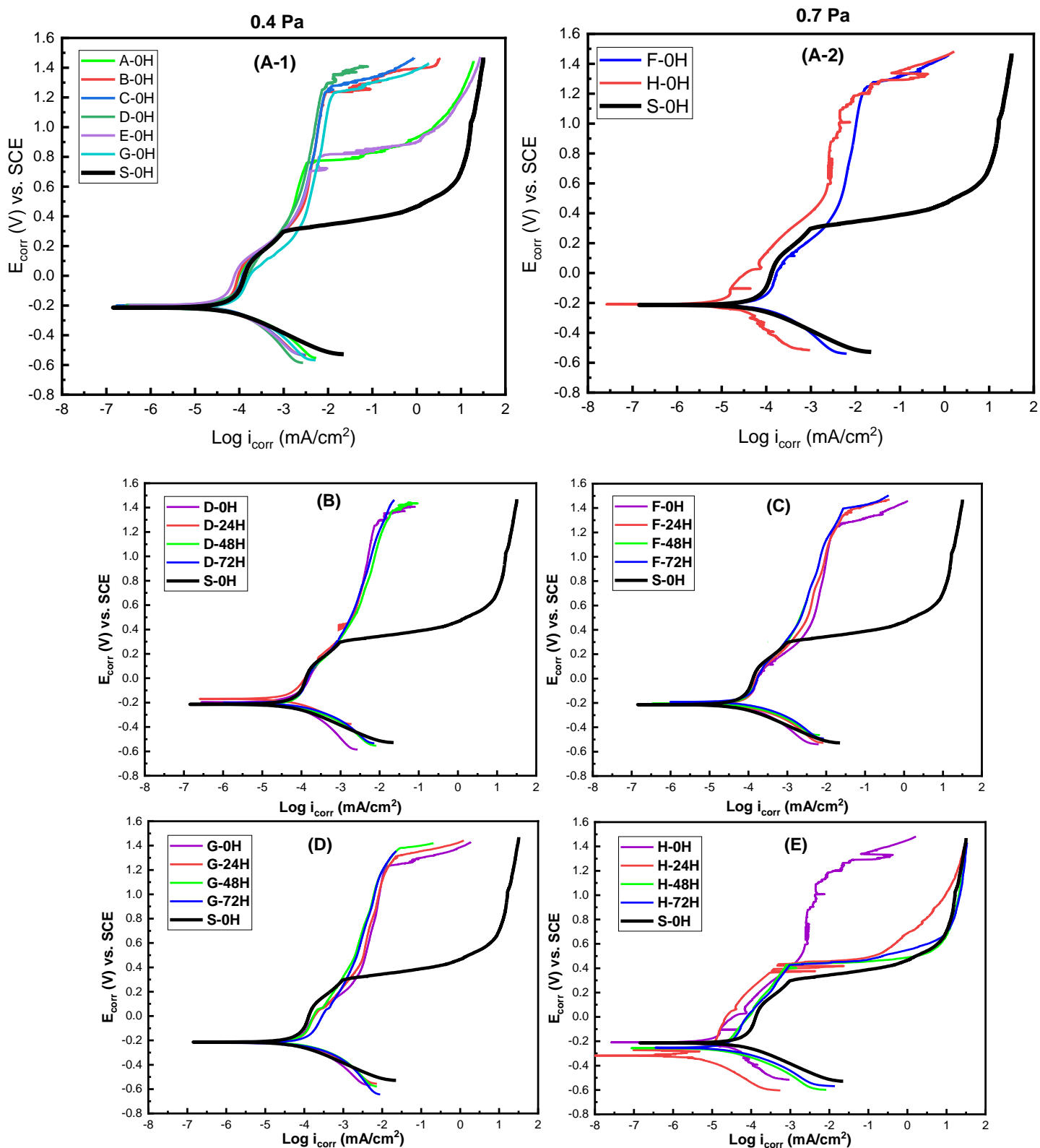
Figure 4.8: *Potentiodynamic polarization curves of all coated samples measured at 0 h (A-1) 0.4 Pa (A-2) 0.7 Pa. DOMS-coated samples measured for long-duration (B) at 0.4 Pa and (C) at 0.7 Pa working pressure. (D) DCMS-coated samples measured for long-duration (D) at 0.4 Pa and (E) 0.7 Pa working pressure.*

*Table 4.2: Potentiodynamic polarization test results*

Samples	E_{corr} (mV)	I_{corr} (nA/cm^2)	B_a (mV/dec)	B_c (mV/dec)	Corrosion rate (10^{-3}) (mmpy)
A-DOMS	-185.47	61	880.1	166.3	1.84
B-DOMS	-190.26	59	955.2	193.1	1.89
C-DOMS	-191.57	68	787.6	207.7	1.93
D-DOMS	-193.01	54	431.9	209.7	1.64
E-DOMS	-181.28	59	737.7	186.8	1.70
F-DOMS	-194.10	96	751.1	194.8	1.97
G-DCMS	-196.06	81	592.7	194.6	2.25
H-DCMS	-193.10	94	380.8	289.5	2.51
S-uncoated	-216.93	82	628.9	628.9	2.83

SEM micrographs were taken to corroborate the effects of corrosion on the coated samples during the immersion in 3.5% NaCl. *Figure 4.9* displays SEM images and EDS results of the corroded surface of all coated samples after 72 h exposure to artificial saline water. The corroded medium severely attacked the surface of all samples. Close examination of the DOMS-coated samples (see *Figure 4.9*A-F) reveals that the surface was attacked by pitting corrosion, but the coating of sample D (300 V, 80% N_2 @ 0.4 Pa) was not damaged due to the dense morphology (see *Figure 4.1*). Also, the robust film was influenced by the strong bonding of Zr–N atoms that prevent defects and cut-off contact with the aggressive electrolyte from the surface [75]. Contrary, the surface of sample F was severely damaged with cracks. The surface cracks damaged the film and allowed the solution to sink into the substrate, causing pitting corrosion. On the other hand, the SEM images of DCMS-coated samples have been shown in *Figure 4.9*G.1-H.1. The crack propagation on the coatings as a function of immersion time can be observed. These cracks allow the penetration of saline solution toward the substrate, further causing the delamination of the protected layer. Looking at EDS analysis (*Figure 4.9*A.1-F.1), the damaged samples reveal major elements like Fe, Cr, and Ni due to delamination of Zr-N film, which exposed the substrate.

The corrosion mechanism of ZrN coatings is displayed in *Figure 4.10*. According to *Figure 4.10a*, the existence of a dense ZrN layer (deposited via DOMS) prevented the contact of aggressive Cl$^-$ ions to the substrate; thus, no detection of pores or micro-cracks (see *Figure 4.10*(a-1)). However, the reaction between the NaCl and substrate has occurred through the

defective surface caused by small pores or droplets, as shown in *Figure 4.10b*. Considering the columnar morphology obtained by DCMS, cracks were initiated from tiny pores, possibly present from deposition (surface defects). Later, those pores joint to form cracks. Apparently, due to an attack of Cl$^-$ ions, the coatings were damaged (see *Figure 4.10*(b-1)), allowing an easier electrolyte sinking, which went through the film to the substrate and eventually, delamination occurred. After the coating delamination, the substrate (316L SS) started to display some pitting corrosion on the surface, which is expected behaviour when SS exposed to "seawater" [76].
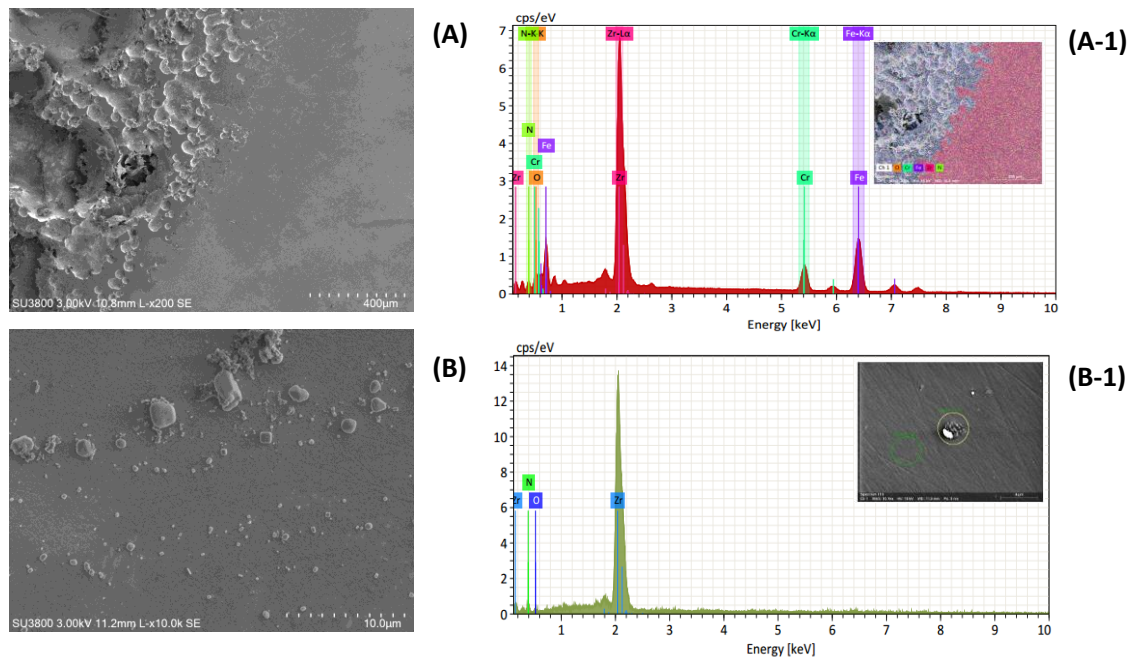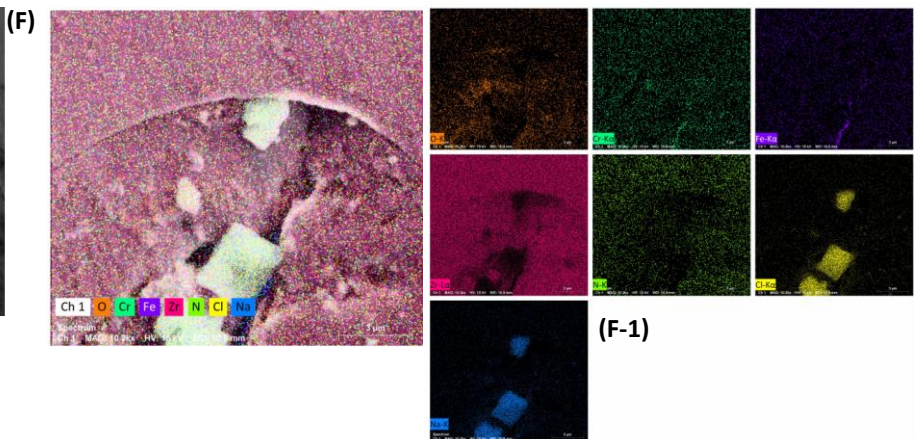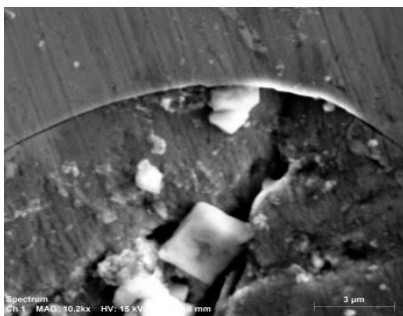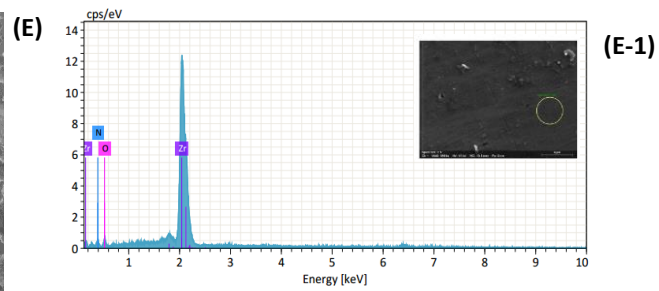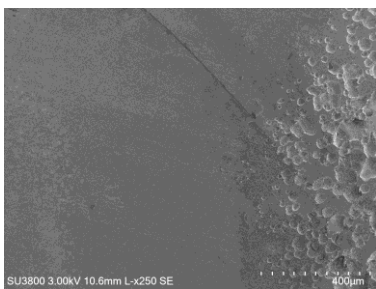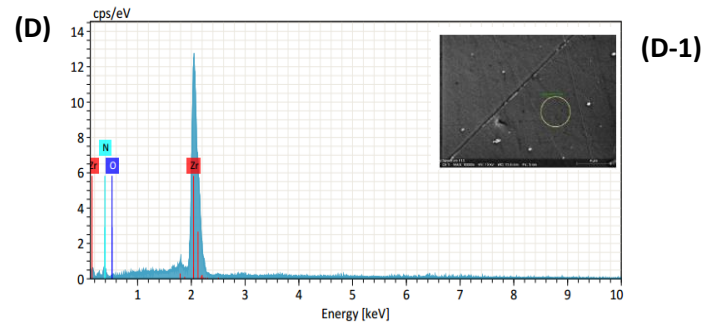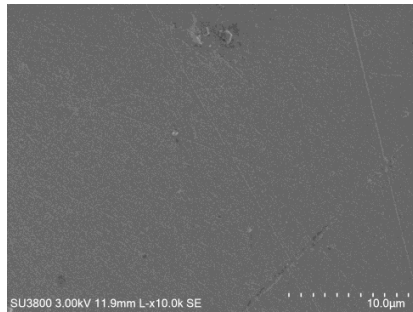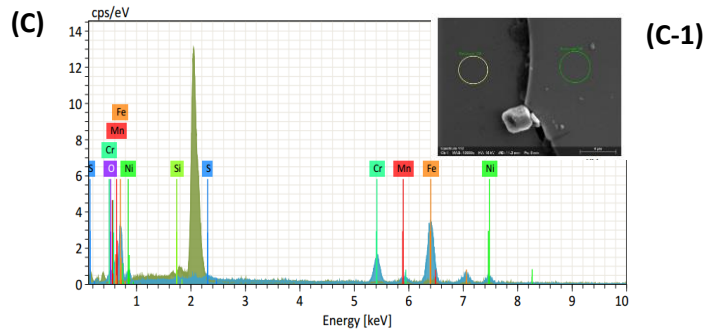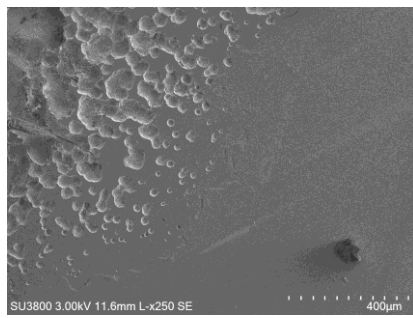
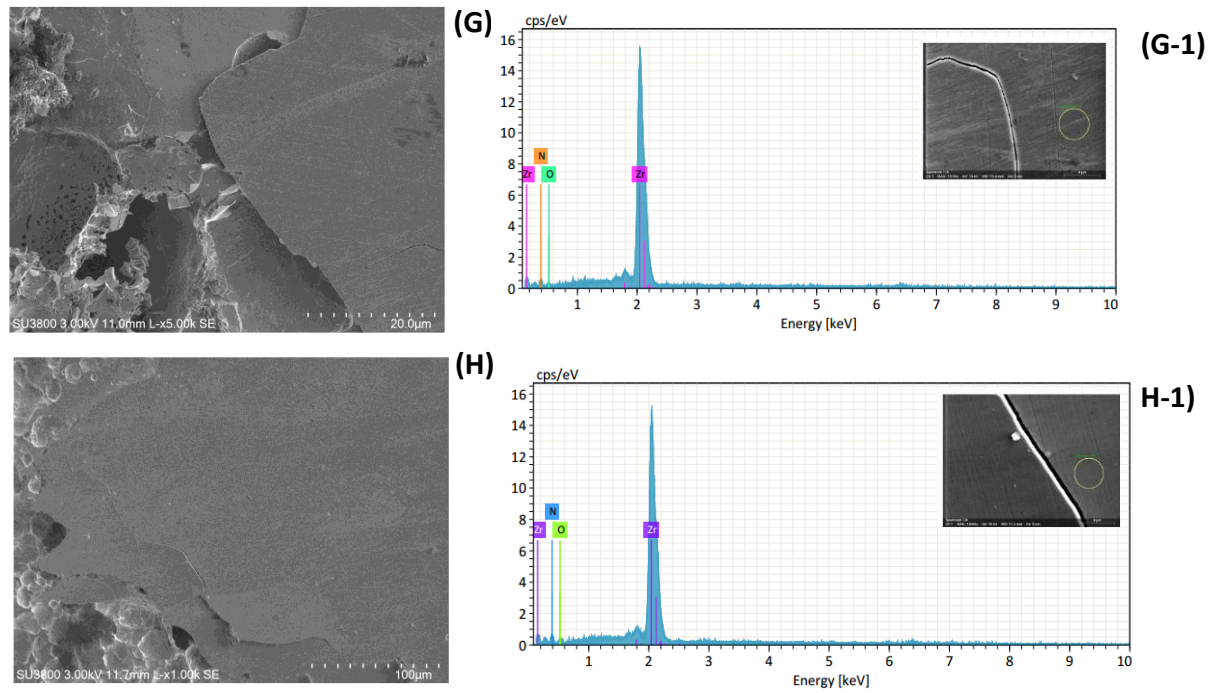**Figure 4.9:** *SEM micrographs of (A-F) DOMS-coated (G,H) DCMS-coated samples exposed to 3.5% NaCl. EDS results of (A.1–F.1) DOMS-coated and (G.1, H.1) DCMS-coated samples. EDS imaged region is given in the inset.*
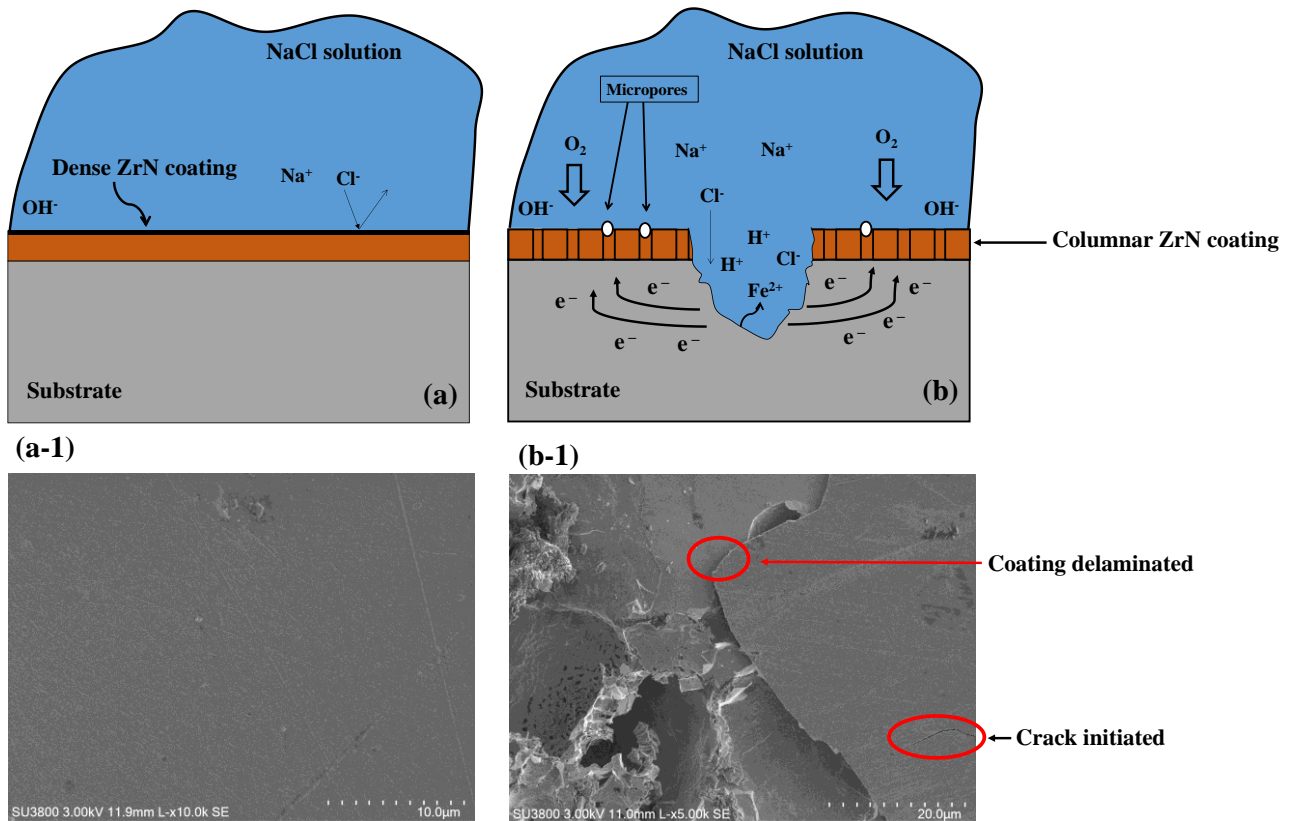

Figure 4.10: *Schematic diagram of the corrosion mechanism of ZrN coatings deposited via (a) DOMS (b) DCMS compared with SEM image of (a-1) dense DOMS-coating and (b-1) DCMS-coating*

4.4. Tribological performance

4.4.1. Coefficient of friction of dry and wet conditioned coatings

The evolution of the coefficient of friction (COF) with two different conditions (dry and wet) in contact with alumina (Al_2O_3) balls using pin-on-disc tests of the ZrN coatings is shown in *Figure 4.11*. Looking at dry condition tests (*Figure 4.11a*), the COF of all coatings ranged between (0.20–0.6). Initially, a running-in period of high values in COF was observed in the first 1000 cycles (40 meters) of the pin-on-disc tests because of severe material transfer during the contact between the alumina ball and the coatings. After this period, a steady-state regime of all tests was reached till the end. It can be seen the trend of friction for all samples is similar except for samples E and F. The COF of sample E gradually increased at the beginning of the sliding test and met the highest value (close to the uncoated substrate) after 1500 cycles because after 1500 cycles the substrate reached the counter body. Initially, sample F shows the lowest COF, which surprisingly increased after 1500 cycles due to the mechanical damage of the film and gave the highest value until the end of 5000 cycles. On the other hand, the wet tests (see *Figure 4.11b*) were conducted in 3.5% NaCl using the same parameters (adopted for dry conditions) to determine the COF of coatings under saline solution (50 mL). It can be observed that COF increases in the beginning for all samples (typical running-in period) until ~500 cycles. After this, a decline in COF was observed, which maintained a steady state until the end of the tests (5000 cycles).

The COF averaged over the last 3000 cycles of sliding (i.e., within the steady-state region), as shown in *Figure 4.12*. The relatively low COF was obtained for the dry-conditioned samples. The least values of DOMS coatings were measured for the samples (A and B) deposited at 0.4 Pa (working pressure) under N_2 flow of 30% and 40%, respectively. At the same time, a higher average COF was measured for the sample (F) deposited at 0.7 Pa (working pressure) under N_2 flow of 50%. On the other hand, the DCMS-coated samples (G and H) unveiled intermediate COF values around 0.43. The dry-conditioned COF value of the uncoated sample showed the highest COF.

The wet wear tests (*Figure 4.12*) revealed higher COF values in comparison to dry-conditioned. Lower COF was obtained for DOMS coatings deposited under low N_2 flow (samples A and B). No significant change is observed for DCMS coatings. It is worth

mentioning that the saline solution had an important influence in the rise of COF. When the pin-on-disc test applies to the coating, the top layer/film starts delamination. If the coating is not strong enough or has inherent defects i.e., pinholes, then the saline solution will penetrate to the substrate, where the localised corrosion mechanism will start [32]. Considering these conditions, Cl^- ions accentuated the corrosion process's intensity, further damaging the substrate underneath the coating [77]. Thus, the blister formation beneath the corrosion products' layers subsequently fractures during the sliding contact when the normal load is applied. However, interestingly least COF discloses on the uncoated sample. This is because the stainless steel forms Cr-oxide over the surface, which protects from unwanted Cl^- ions to attacking it [16].
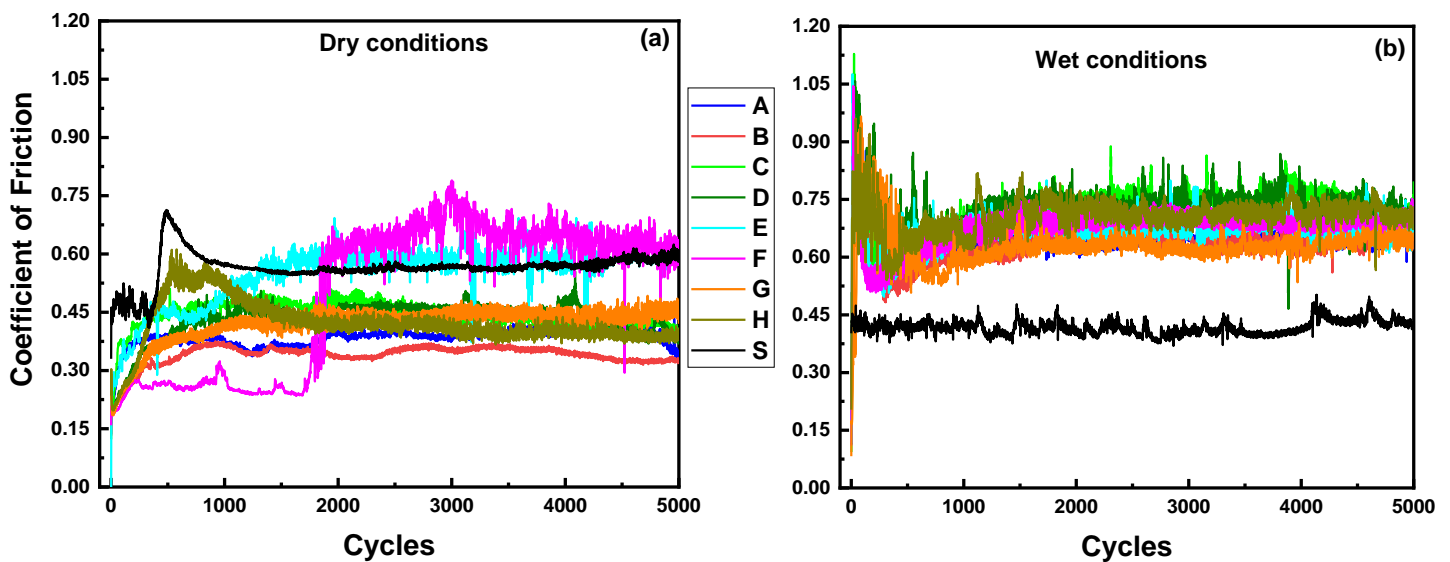

Figure 4.11: *Coefficient of friction of (a) dry and (b) wet condition tests of DOMS-coated (A-F), (G-H) DCMS-coated samples, and (S) uncoated substrate with tribological contact of 10 mm Al₂O₃ ball performed via pin and disc test under 2 N load and 200 m distance.*
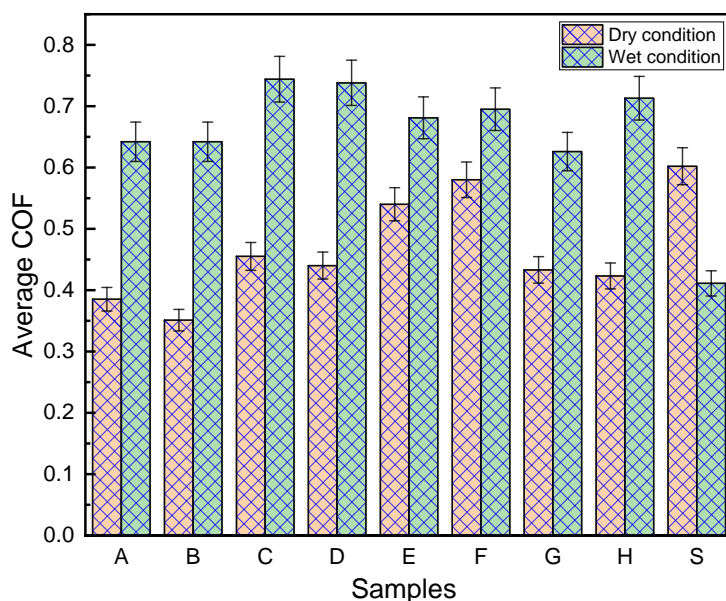
Figure 4.12: *Average COF of dry and wet conditioned samples (A-F) DOMS-coated samples (G,H), DCMS-coated samples (S), uncoated substrate*

4.4.2. 2D profiles of wet and dry conditioned coatings

2D profiles of wear track (dry conditioned) coatings were collected after the pin-on-disc test, as shown in *Figure 4.13*. It can be seen that the counter body (alumina ball) penetrated very deep (~10 μm) into the uncoated sample (S). Comparing the coated samples' profiles, a compromising outcome is observed on DOMS coating (sample C), which was deposited under 60% N_2 flow @ 0.4 Pa working pressure. The wear track is shallow (less than the coating thickness, i.e., 1 μm), showing greater wear resistance properties. Looking at the depth profile of the highest damaged surface (sample F), a deep track (equivalent to the uncoated substrate) is obtained. Meaning that the DOMS-coating carried out at 250 V, under 50% N_2 flow @ 0.4 Pa working pressure is completely delaminated (unable to protect the substrate), which agrees with the result shown in *Figure 4.11a*. The results propose that moderate N_2 flow @ 0.4 Pa working pressure can significantly improve the mechanical properties (hardness) of the film applied via DOMS technique. Increasing N_2 flux and working pressure could not provide good mechanical properties in the deposition process [68, 69]. Huang et al. [68] reported that increasing N_2 flow in the ZrN coatings affect the packing factor of compact morphology in the ZrN films which directly increase the residual stress. The residual stresses can harm the mechanical properties (hardness) during the sliding actions. Concerning the DCMS-coated samples, a deep valley for sample H (50% N_2 flow

@0.7 Pa working pressure) can be seen in 2D profiles. This means that the coating delaminated from the substrate.

Figure 4.14 shows 2D profiles of wet conditioned coated (DOMS and DCMS) samples compared with the uncoated substrate (S). It is worth noting that coatings deposited with both techniques were somehow damaged and could not withstand friction force because the counter body penetrated deeper than dry conditions (see *Figure 4.14*). Incorporating N_2 at various percentages, changing target peak power and working pressure significantly influence the properties under aggressive saline solution. However, comparing DOMS coatings (A-F) with DCMS (G,H), higher depth profiles are observed on DCMS coatings. Meaning that the columnar morphology of ZrN could not prevent mechanical forces during the test and the saline solution sinks to the substrate through tiny holes/cracks [70]. It can be concluded that Cl$^-$ ions attacked more underneath the DCMS coatings (similar mechanism as explained before) and thus could not protect the substrate against sliding contact during the pin-on-disc test (performed in 3.5% NaCl) [44]. On the other hand, uncoated substrate reached a depth of ~10 μm.
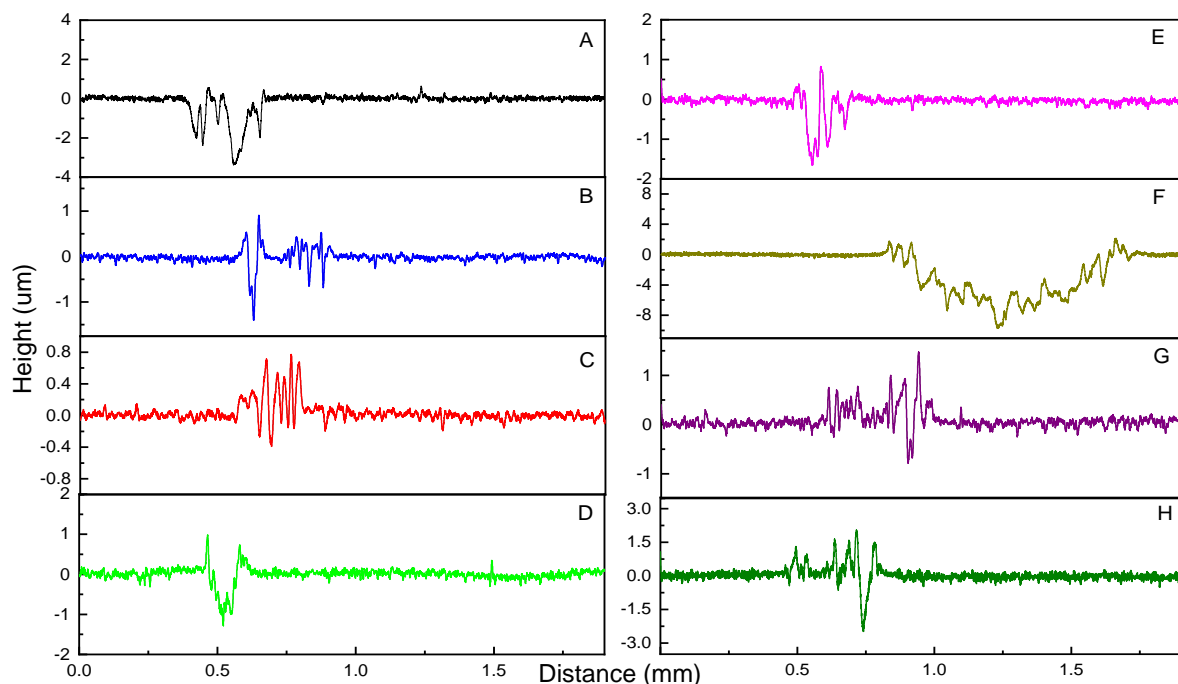
Figure 4.13: *2D profiles of wear track of dry sample deposited via (A-F) DOMS and (G,H) DCMS in dry condition (S) uncoated samples.*

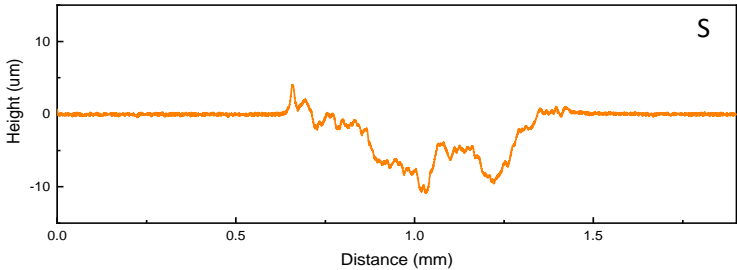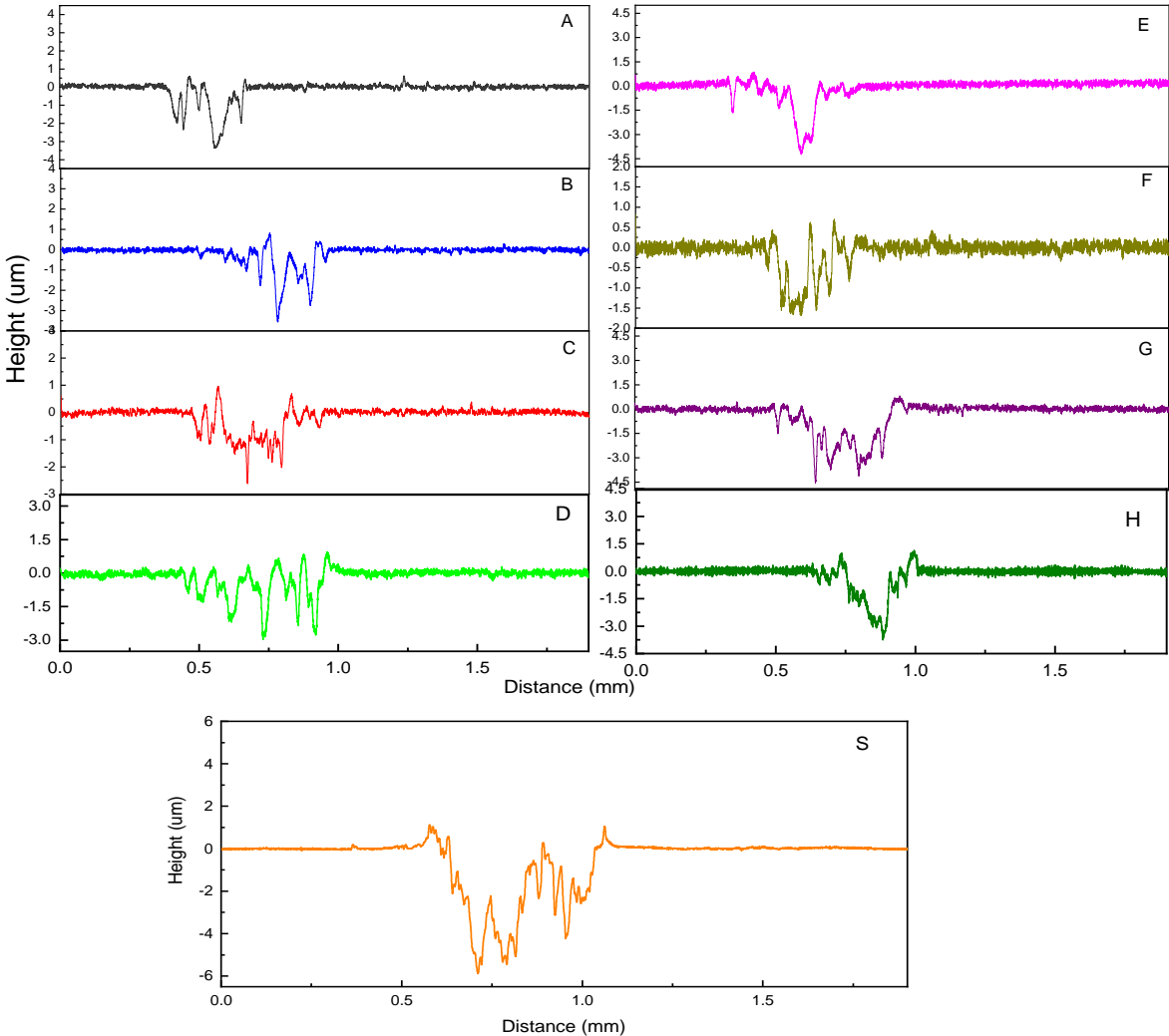***Figure 4.14:*** *2D profiles of wear track of dry sample deposited via (A-F) DOMS and (G,H) DCMS in wet condition (S) uncoated samples.*

4.4.3. Wear analysis of dry and wet conditioned coatings

The wear rates were calculated employing the eq. (3) [78]. *Figure 4.15* shows the wear rate of DOMS and DCMS coatings compared with the uncoated samples in dry and

wet conditions. Dry condition coatings have lower wear rates except the coating (sample F) deposited with 250 V, 50% N_2 flow @ 0.7 Pa working pressure. As described previously, the high working pressure with low peak power could not deliver a hard wear-resistant film. By adjusting the voltages (300 V) at moderate N_2 flux (60%) under low working pressure (0.4 Pa), we have achieved high wear resistant ZrN coating (sample C) via the DOMS technology. In contrast, DCMS coatings (samples G and H) delivered high wear rates in dry conditions (see *Figure 4.15*). Looking at wear rates of wet condition coatings, a similar trend on all coatings is disclosed as we have discussed for dry conditions. These results are consistent with 2D depth profiles. The uncoated samples have the highest wear rate in both dry and wet conditions.

Lastly, the wear tracks and the elemental composition of damaged coatings were measured and compared with protected sample, as shown in *Figure 4.16*. The primary wear behaviour of both conditions (dry and wet) appears to be abrasion. DOMS-coated samples (*Figure 4.16*C) show fewer scratches and grooves as a function of sliding action due to the presence of dense ZrN films. The red arrow shows wear debris during rubbing, while the blue arrow represents non-damaged region. The EDS analysis shows that the counter body could not reach the substrate during pin-on-disc test. Nevertheless, deep furrows scratched from trapped particles can be seen on samples (*Figure 4.16*E,F). EDS's detection of Fe, Cr, and Ni (main elements present in stainless steel) reveals that the counter body reached the substrate as a function of sliding action. Severe wear debris as a function of sliding action can be seen with yellow circle. DCMS-coated sample (*Figure 4.16*G) exhibited highest wear track and severe damaged coating. From the wear rates and SEM results, we can conclude that the wear mechanism could not damage the ZrN film (sample C) deposited under optimum conditions (300 V, 60% N_2 flow @ 0.4 Pa working pressure) via DOMS technique.
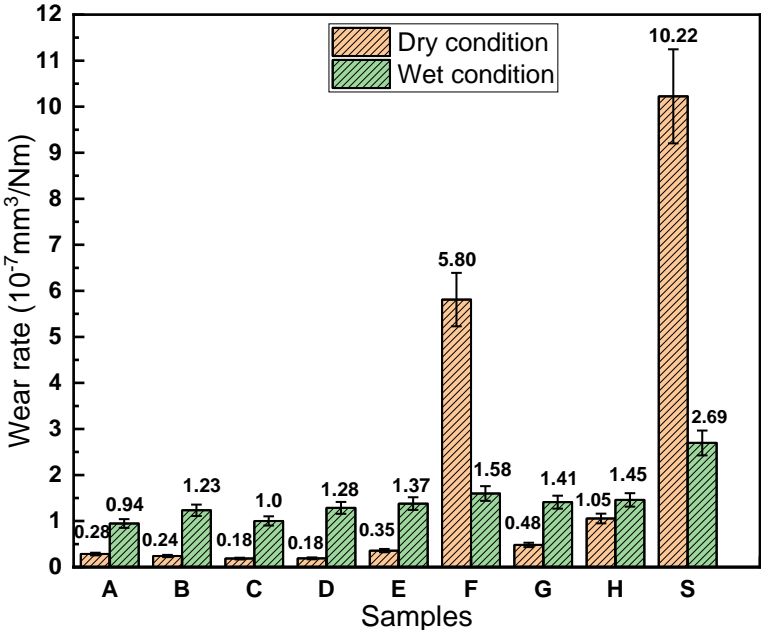
Figure 4.15: *Wear rate of DOMS-coated (A-F) and DCMS-coated (G, H) samples as a function of dry and wet conditions compared with uncoated sample (S)*
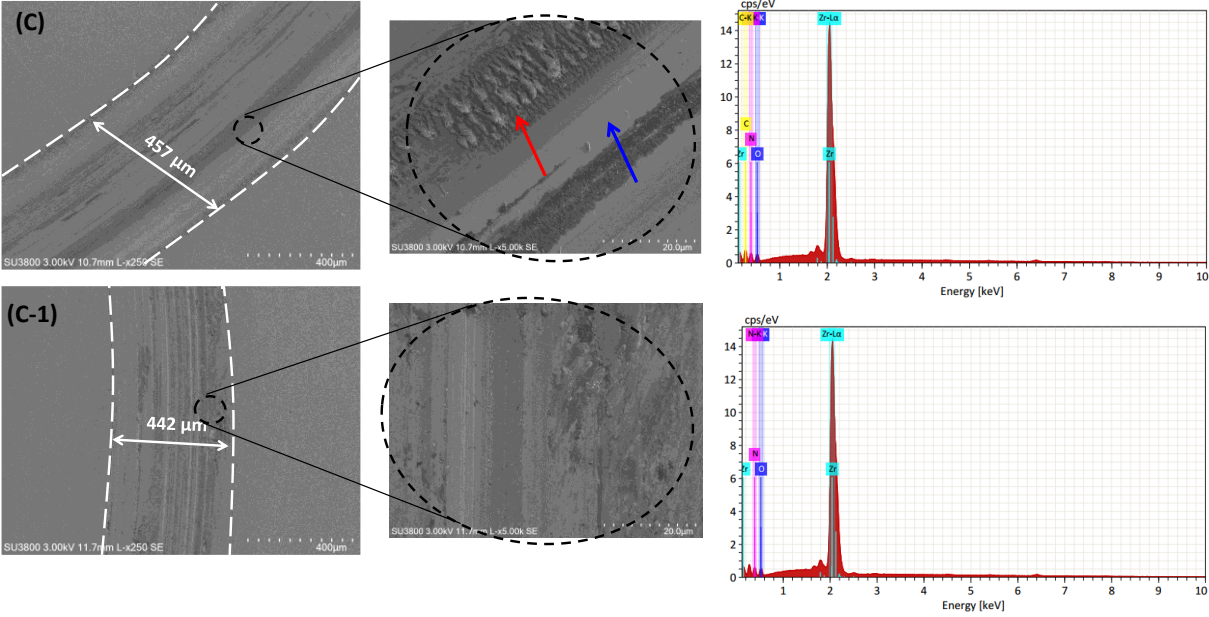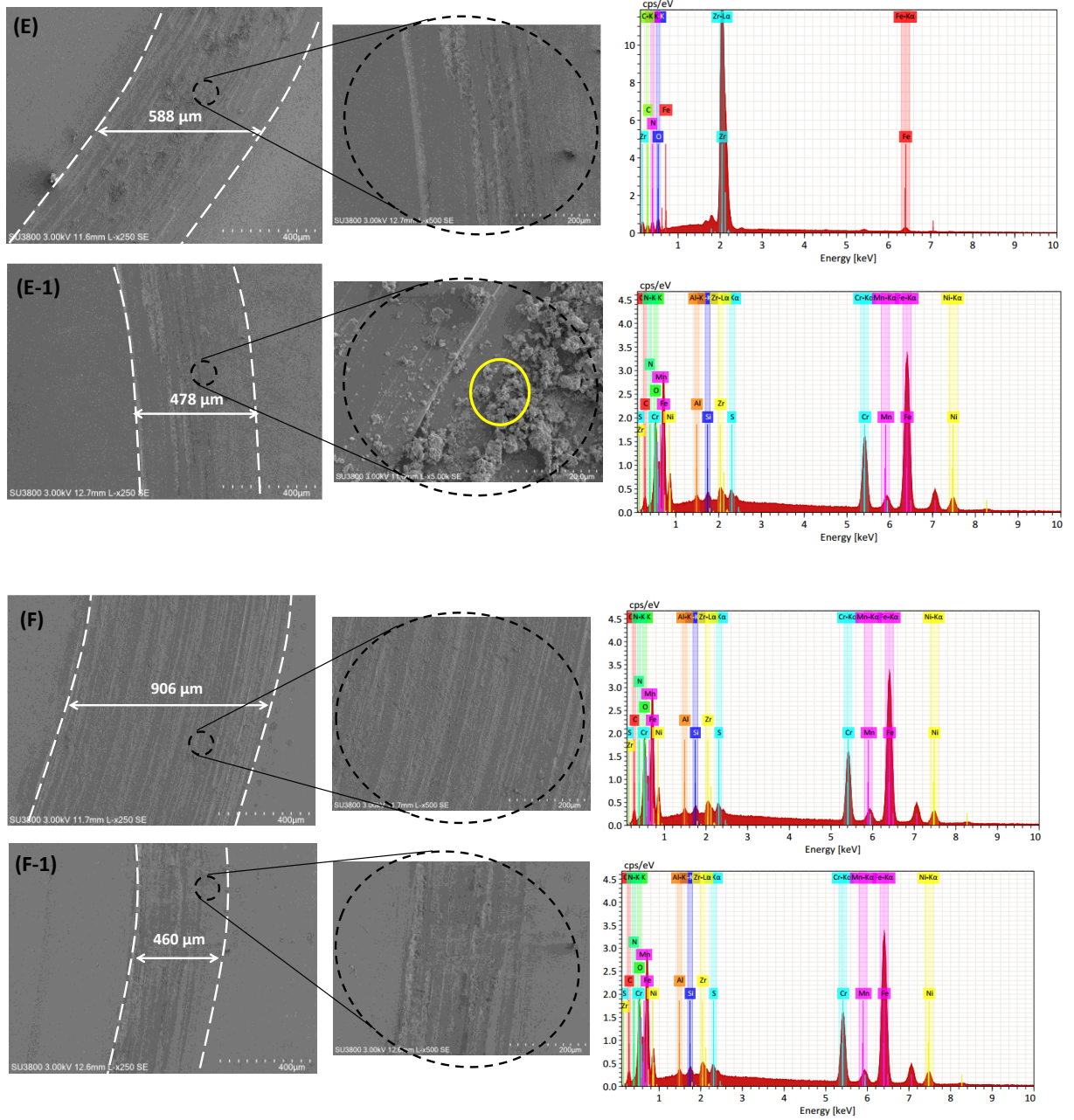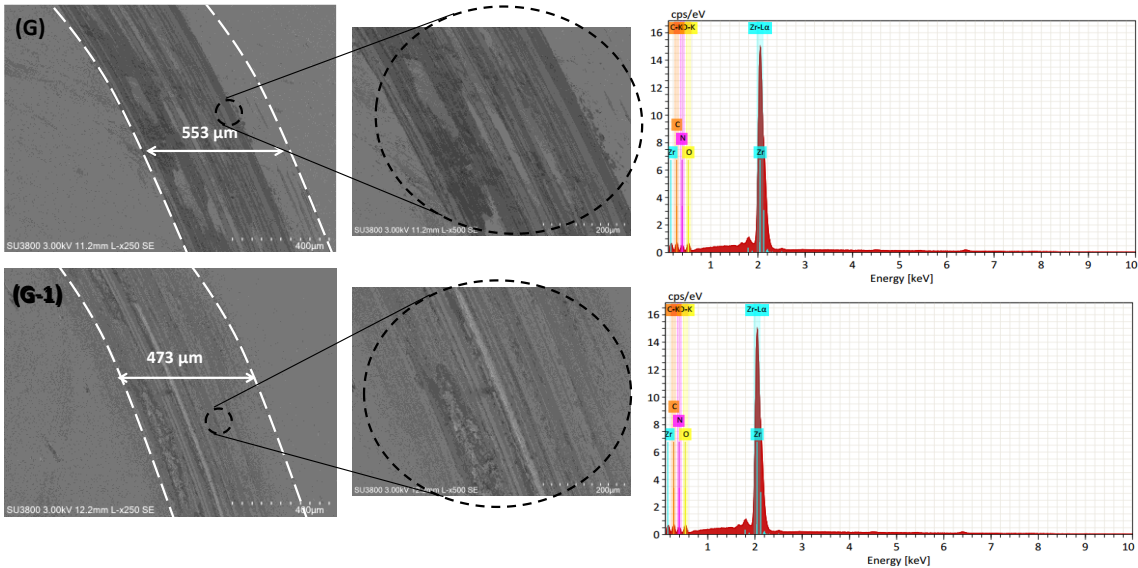
Figure 4.16: *Wear track of (C,E and F) DOMS-coated and (G) DCMS-coated samples in dry condition. Wear track of (C-1,E-1 and F-1) DOMS-coated and (G-1) DCMS-coated samples in wet condition along with EDS analysis.*

CHAPTER 5

5. CONCLUSIONS

ZrN-based coatings were performed on stainless steel substrate under several optimum conditions using DOMS technique and compared them with DCMS coatings. The following outcomes of corrosion and tribological analysis are demonstrated:

➢ DOMS coatings delivered dense and compact morphology to ZrN coatings of ~1 μm, while columnar and cauliflower-type coatings were achieved by DCMS deposition.

➢ EIS results revealed the highest impedance of DOMS coatings carried out at 300 V, 80% N_2 flow and at 0.4 Pa working pressure.

➢ Potentiodynamic polarization curves have shown the least corrosion rates on ZrN film of DOMS-coated sample (300 V, 80% N_2 flow at 0.4 Pa working pressure) for 72 h.

➢ The wet conditioned wear test unveiled that the samples obtained higher COF than the dry tests. Apparently, Cl^- ions attacked the substrate underneath the deposited films carried out via DCMS technology.

➢ The lower wear rates of coatings were obtained on the samples deposited by DOMS in both dry and wet conditions.

6. FUTURE WORK

- ❖ Optimization of deposition parameters, such as changing the bias voltages and carrying gas inside the sputtering chamber.
- ❖ Tribocorossion tests to evaluate the synergy between corrosion and mechanical wear.

REFERENCES

1.   MacLeod, L.D., 1989. The application of corrosion science to the management of maritime archaeological sites. *Bulletin of the Australian Institute for Maritime Archaeology, The*, *13*(2), pp.7-16.

2.   Lian, J.S., Li, G.Y., Niu, L.Y., Gu, C.D., Jiang, Z.H. and Jiang, Q., 2006. Electroless Ni–P deposition plus zinc phosphate coating on AZ91D magnesium alloy. *Surface and Coatings Technology*, *200*(20-21), pp.5956-5962.

3.   Lin, Z.F., Zhang, D., Wang, Y. and Wang, P., 2012. A zinc/silicon dioxide composite film: Fabrication and anti-corrosion characterization. *Materials and Corrosion*, *63*(5), pp.416-420.

4.   Barik, R.C., Wharton, J.A., Wood, R.J.K., Stokes, K.R. and Jones, R.L., 2005. Corrosion, erosion and erosion–corrosion performance of plasma electrolytic oxidation (PEO) deposited Al2O3 coatings. *Surface and coatings technology*, *199*(2-3), pp.158-167.

5.   Alves, A.C., Wenger, F., Ponthiaux, P., Celis, J.P., Pinto, A.M., Rocha, L.A. and Fernandes, J.C.S., 2017. Corrosion mechanisms in titanium oxide-based films produced by anodic treatment. *Electrochimica Acta*, *234*, pp.16-27.

6.   Teixeira, V., Monteiro, A., Duarte, J. and Portinha, A., 2002. Deposition of composite and nanolaminate ceramic coatings by sputtering. *Vacuum*, *67*(3-4), pp.477-483.

7.   Milošev, I. and G. Frankel, *Conversion coatings based on zirconium and/or titanium.* Journal of The Electrochemical Society, 2018. **165**(3): p. C127.

8.   Gao, Z., Chen, Y., Kulczyk-Malecka, J., Kelly, P., Zeng, Y., Zhang, X., Li, C., Liu, H., Rohbeck, N. and Xiao, P., 2018. Comparison of the oxidation behavior of a zirconium nitride coating in water vapor and air at high temperature. *Corrosion Science*, *138*, pp.242-251.

9.   Muboyadzhyan, S.A., 2009. Erosion-resistant coatings for gas turbine compressor blades. *Russian Metallurgy (Metally)*, *2009*(3), pp.183-196.

10. Sarakinos, K., J. Alami, and S. Konstantinidis, *High power pulsed magnetron sputtering: A review on scientific and engineering state of the art.* Surface and Coatings Technology, 2010. **204**(11): p. 1661-1684.

11. Alami, J., Sarakinos, K., Mark, G. and Wuttig, M., 2006. On the deposition rate in a high power pulsed magnetron sputtering discharge. *Applied physics letters*, *89*(15), p.154104.

12. Nakao, S., Yukimura, K., Nakano, S. and Ogiso, H., 2013. DLC coating by HiPIMS: The influence of substrate bias voltage. *IEEE transactions on plasma science*, *41*(8), pp.1819-1829.

13. PalDey, S.C.D.S. and Deevi, S.C., 2003. Single layer and multilayer wear resistant coatings of (Ti, Al) N: a review. *Materials Science and Engineering: A*, *342*(1-2), pp.58-79.

14. Danek Jr, G.J., 1966. The Effect of Sea-Water Velocity on the Corrosion Behavior of Metals. *Naval Engineers Journal*, *78*(5), pp.763-769.

15. Hou, X., Gao, L., Cui, Z. and Yin, J., 2018. Corrosion and protection of metal in the seawater desalination. In *IOP conference series: earth and environmental science* (Vol. 108, No. 2, p. 022037). IOP Publishing.

16. Pacquentin, W., Caron, N. and Oltra, R., 2015. Effect of microstructure and chemical composition on localized corrosion resistance of a AISI 304L stainless steel after nanopulsed-laser surface melting. *Applied Surface Science*, *356*, pp.561-573.

17. Yin, F.L., Ji, H. and Nie, S.L., 2019. Tribological behavior of various ceramic materials sliding against CF/PTFE/graphite-filled PEEK under seawater lubrication. *Proceedings of the Institution of Mechanical Engineers, Part J: Journal of Engineering Tribology*, *233*(11), pp.1729-1742.

18. Mills, D.J. and Knutsen, R.D., 1998. An investigation of the tribological behaviour of a high-nitrogen CrMn austenitic stainless steel. *Wear*, *215*(1-2), pp.83-90.

19. Shin, J.H. and Lee, J.W., 2014. Effects of twin intersection on the tensile behavior in high nitrogen austenitic stainless steel. *Materials characterization*, *91*, pp.19-25.

20. Barbangelo, A., 1990. Influence of alloying elements and heat treatment on impact toughness of chromium steel surface deposits. *Journal of materials science*, *25*(6), pp.2975-2984.

21. Zhao, E. and Wu, Z., 2008. Electronic and mechanical properties of 5d transition metal mononitrides via first principles. *Journal of Solid State Chemistry*, *181*(10), pp.2814-2827.

22. Zhang, Z.G., Rapaud, O., Allain, N., Mercs, D., Baraket, M., Dong, C. and Coddet, C., 2009. Microstructures and tribological properties of CrN/ZrN nanoscale multilayer coatings. *Applied Surface Science*, *255*(7), pp.4020-4026.

23. Wang, B., Su, Y., Tian, L., Peng, S. and Ji, R., 2020. Heavy metals in face paints: Assessment of the health risks to Chinese opera actors. *Science of The Total Environment*, *724*, p.138163.

24. Hofer, A.M., Mori, G., Fian, A., Winkler, J. and Mitterer, C., 2016. Improvement of oxidation and corrosion resistance of Mo thin films by alloying with Ta. *Thin Solid Films*, *599*, pp.1-6.

25. Haq, M.I.U., Raina, A., Vohra, K., Kumar, R. and Anand, A., 2018. An assessment of tribological characteristics of different materials under sea water environment. *Materials Today: Proceedings*, *5*(2), pp.3602-3609.

26. Zhao, L., Yao, X., Hang, R., Zhang, X. and Tang, B., 2018. Corrosion behavior of porous ZrO2 ceramic coating on AZ31B magnesium alloy. *Surface and Coatings Technology*, *349*, pp.434-441.

27. Vathsala, K. and Venkatesha, T.V., 2011. Zn–ZrO2 nanocomposite coatings: Elecrodeposition and evaluation of corrosion resistance. *Applied Surface Science*, *257*(21), pp.8929-8936.

28. Setiawan, A.R., Noorprajuda, M., Ramelan, A. and Suratman, R., 2015. Preparation of Zn-ZrO2 Nanocomposite Coating by DC and Pulsed Current Electrodeposition Technique with Low Current Density. In *Materials Science Forum* (Vol. 827, pp. 332-337). Trans Tech Publications Ltd.

29. Kuznetsova, T., Lapitskaya, V., Khabarava, A., Chizhik, S., Warcholinski, B. and Gilewicz, A., 2020. The influence of nitrogen on the morphology of ZrN coatings deposited by magnetron sputtering. *Applied Surface Science*, *522*, p.146508.

30. Ul-Hamid, A., 2020. Microstructure, properties and applications of Zr-carbide, Zr-nitride and Zr-carbonitride coatings: A review. *Materials Advances*, *1*(5), pp.1012-1037.

31. Chou, W.J., Yu, G.P. and Huang, J.H., 2003. Corrosion resistance of ZrN films on AISI 304 stainless steel substrate. *Surface and Coatings Technology*, *167*(1), pp.59-67.

32. Staia, M.H., Trocelis, A., Zairi, A., Suarez, M., Puchi-Cabrera, E.S., Iost, A. and Montagne, A., 2019. Assessment of the mechanical and tribological performance of a ZrN PVD coating. *Surface Engineering*, *35*(6), pp.491-500.

33. Rizzo, A., Signore, M.A., Mirenghi, L. and Di Luccio, T., 2009. Synthesis and characterization of titanium and zirconium oxynitride coatings. *Thin Solid Films*, *517*(21), pp.5956-5964.

34. Hill, W.L., Vogel, E.M., Misra, V., McLarty, P.K. and Wortman, J.J., 1996. Low-pressure rapid thermal chemical vapor deposition of oxynitride gate dielectrics for n-channel and p-channel MOSFETs. *IEEE Transactions on Electron Devices*, *43*(1), pp.15-22.

35. Ariza, E., Rocha, L.A., Vaz, F., Cunha, L., Ferreira, S.C., Carvalho, P., Rebouta, L., Alves, E., Goudeau, P. and Rivière, J.P., 2004. Corrosion resistance of ZrNxOy thin films obtained by rf reactive magnetron sputtering. *Thin Solid Films*, *469*, pp.274-281.

36. Muboyadzhyan, S.A., 2011. Erosion-resistant metal nitride coatings and carbide and their plasmochemical synthesis. *Russian Journal of General Chemistry*, *81*(5), pp.1053-1060.

37. Sue, J.A. and Troue, H.H., 1991. High temperature erosion behavior of titanium nitride and zirconium nitride coatings. *Surface and coatings technology*, *49*(1-3), pp.31-39.

38. Rie, K.T., Gebauer, A. and Wöhle, J., 1996. Plasma assisted CVD for low temperature coatings to improve the wear and corrosion resistance. *Surface and Coatings Technology*, *86*, pp.498-506.

39. Rie, K.T. and Wöhle, J., 1999. Plasma-CVD of TiCN and ZrCN films on light metals. *Surface and Coatings Technology*, *112*(1-3), pp.226-229.

40. Roman, D., Bernardi, J., de Amorim, C.L., de Souza, F.S., Spinelli, A., Giacomelli, C., Figueroa, C.A., Baumvol, I.J. and Basso, R.L., 2011. Effect of deposition temperature on microstructure and corrosion resistance of ZrN thin films deposited by DC reactive magnetron sputtering. *Materials Chemistry and Physics*, *130*(1-2), pp.147-153.

41. Wang, Y., Liu, Q., Liu, J., Zhang, L. and Cheng, L., 2008. Deposition mechanism for chemical vapor deposition of zirconium carbide coatings. *Journal of the American Ceramic Society*, *91*(4), pp.1249-1252.

42. Silva, E., de Figueiredo, M.R., Franz, R., Galindo, R.E., Palacio, C., Espinosa, A., Mitterer, C. and Carvalho, S., 2010. Structure–property relations in ZrCN coatings for tribological applications. *Surface and Coatings Technology*, *205*(7), pp.2134-2141.

43. Budke, E., Krempel-Hesse, J., Maidhof, H. and Schüssler, H., 1999. Decorative hard coatings with improved corrosion resistance. *Surface and Coatings Technology*, *112*(1-3), pp.108-113.

44. Gu, J.D. and Chen, P.L., 2006. Investigation of the corrosion resistance of ZrCN hard coatings fabricated by advanced controlled arc plasma deposition. *Surface and Coatings Technology*, *200*(10), pp.3341-3346.

45. Ferreira, C.P., Castro, M.D.M.R.D., Tentardini, E.K., Lins, V.D.F.C. and Saliba, P.A., 2020. Silicon influence on corrosion resistance of magnetron sputtered ZrN and ZrSiN thin films. *Surface Engineering*, *36*(1), pp.33-40.

46. Yan, L., Zhang, X., Hu, P., Zhao, G., Dong, S., Liu, D., Sun, B., Zhang, D. and Han, J., 2017. Carbon nanofiber arrays grown on three-dimensional carbon fiber architecture substrate and enhanced interface performance of carbon fiber and zirconium carbide coating. *ACS Applied Materials & Interfaces*, *9*(20), pp.17337-17346.

47. Braic, M., Braic, V., Balaceanu, M., Zoita, C.N., Kiss, A., Vladescu, A., Popescu, A. and Ripeanu, R., 2011. Structure and properties of Zr/ZrCN coatings deposited by cathodic arc method. *Materials Chemistry and Physics*, *126*(3), pp.818-825.

48. Chen, S.F., Kuo, Y.C., Wang, C.J., Huang, S.H., Lee, J.W., Chan, Y.C., Chen, H.W., Duh, J.G. and Hsieh, T.E., 2013. The effect of Cr/Zr chemical composition ratios on the mechanical properties of CrN/ZrN multilayered coatings deposited by cathodic arc deposition system. *Surface and Coatings Technology*, *231*, pp.247-252.

49. Ul-Hamid, A., 2020. The effect of deposition conditions on the properties of Zr-carbide, Zr-nitride and Zr-carbonitride coatings–a review. *Materials Advances*, *1*(5), pp.988-1011.

50. Craciun, D., Socol, G., Dorcioman, G., Stefan, N., Bourne, G. and Craciun, V., 2009. High quality ZrC, ZrC/ZrN and ZrC/TiN thin films grown by pulsed laser deposition. *Journal of Optoelectronics and Advanced Materials*, *12*(March 2010), pp.461-465.

51. Long, Y., Javed, A., Chen, J., Chen, Z.K. and Xiong, X., 2014. Phase composition, microstructure and mechanical properties of ZrC coatings produced by chemical vapor deposition. *Ceramics International*, *40*(1), pp.707-713.

52. Dubey, P., Arya, V., Srivastava, S., Singh, D. and Chandra, R., 2013. Effect of nitrogen flow rate on structural and mechanical properties of Zirconium Tungsten Nitride (Zr–W–N) coatings deposited by magnetron sputtering. *Surface and Coatings Technology*, *236*, pp.182-187.

53. Cubillos, G.I., Bethencourt, M. and Olaya, J.J., 2015. Corrosion resistance of zirconium oxynitride coatings deposited via DC unbalanced magnetron sputtering and spray pyrolysis-nitriding. *Applied Surface Science*, *327*, pp.288-295.

54. Ramana, J.V., Kumar, S., David, C., Ray, A.K. and Raju, V.S., 2000. Characterisation of zirconium nitride coatings prepared by DC magnetron sputtering. *Materials Letters*, *43*(1-2), pp.73-76.

55. Bräuer, G., Szyszka, B., Vergöhl, M. and Bandorf, R., 2010. Magnetron sputtering–Milestones of 30 years. *Vacuum*, *84*(12), pp.1354-1359.

56. Christou, C. and Barber, Z.H., 2000. Ionization of sputtered material in a planar magnetron discharge. *Journal of Vacuum Science & Technology A: Vacuum, Surfaces, and Films*, *18*(6), pp.2897-2907.

57. Mattox, D.M., 2010. *Handbook of physical vapor deposition (PVD) processing*. William Andrew.

58. Auciello, O. and Kelly, R., 1984. Ion bombardment modification of surfaces.

59. Petrov, I., Barna, P.B., Hultman, L. and Greene, J.E., 2003. Microstructural evolution during film growth. *Journal of Vacuum Science & Technology A: Vacuum, Surfaces, and Films*, *21*(5), pp.S117-S128.

60. Wang, Y.X., Pan, Z.Y., Ho, Y.K., Xu, Y. and Du, A.J., 2001. Nuclear instruments and methods in physics research section B: beam interactions with materials and

atoms. *Nuclear Instruments and Methods in Physics Research B*, *180*(1-4), pp.251-256.

61. Munoz, R.C., Finger, R., Arenas, C., Kremer, G. and Moraga, L., 2002. Surface-induced resistivity of thin metallic films bounded by a rough fractal surface. *Physical Review B*, *66*(20), p.205401.

62. Thornton, J.A., 1974. Influence of apparatus geometry and deposition conditions on the structure and topography of thick sputtered coatings. *Journal of Vacuum Science and Technology*, *11*(4), pp.666-670.

63. Messier, R.A.R.R., Giri, A.P. and Roy, R.A., 1984. Revised structure zone model for thin film physical structure. *Journal of Vacuum Science & Technology A: Vacuum, Surfaces, and Films*, *2*(2), pp.500-503.

64. Anders, A., 2010. A structure zone diagram including plasma-based deposition and ion etching. *Thin Solid Films*, *518*(15), pp.4087-4090.

65. Elmkhah, H., Attarzadeh, F., Fattah-Alhosseini, A. and Kim, K.H., 2018. Microstructural and electrochemical comparison between TiN coatings deposited through HIPIMS and DCMS techniques. *journal of Alloys and Compounds*, *735*, pp.422-429.

66. Hála, M., Čapek, J., Zabeida, O., Klemberg-Sapieha, J.E. and Martinu, L., 2012. Hysteresis-free deposition of niobium oxide films by HiPIMS using different pulse management strategies. *Journal of Physics D: Applied Physics*, *45*(5), p.055204.

67. Ghailane, A., Larhlimi, H., Tamraoui, Y., Makha, M., Busch, H., Fischer, C.B. and Alami, J., 2020. The effect of magnetic field configuration on structural and mechanical properties of TiN coatings deposited by HiPIMS and dcMS. *Surface and Coatings Technology*, *404*, p.126572.

68. Huang, J.H., Ho, C.H. and Yu, G.P., 2007. Effect of nitrogen flow rate on the structure and mechanical properties of ZrN thin films on Si (1 0 0) and stainless steel substrates. *Materials chemistry and physics*, *102*(1), pp.31-38.

69. Ke, Y.E. and Chen, Y.I., 2020. Effects of Nitrogen Flow Ratio on Structures, Bonding Characteristics, and Mechanical Properties of ZrN x Films. *Coatings*, *10*(5), p.476.

70. Ramoul, C., Beliardouh, N.E., Bahi, R., Nouveau, C., Djahoudi, A. and Walock, M.J., 2019. Surface performances of PVD ZrN coatings in biological environments. *Tribology-Materials, Surfaces & Interfaces*, *13*(1), pp.12-19.

71. Subramanian, B., Swaminathan, V. and Jayachandran, M., 2012. Microstructural, tribological and electrochemical corrosion studies on reactive DC magnetron sputtered zirconium nitride films with Zr interlayer on steel. *Metals and Materials International*, *18*(6), pp.957-964.

72. Bai, L., Feng, L.J., Wang, H.Y., Lu, Y.B., Lei, X.W. and Bai, F.L., 2015. Comparison of the synergistic effect of counterions on the inhibition of mild steel corrosion in acid solution: electrochemical, gravimetric and thermodynamic studies. *RSC Advances*, *5*(6), pp.4716-4726.

73. A Arunachalamsugumaran, A., Purandare, Y., Ehiasarian, A. and Hovsepian, P., 2017. Corrosion behaviour of post-deposition polished droplets-embedded arc evaporated and droplets-free HIPIMS/DCMS coatings. *Corrosion*, *73*, pp.685-693.

74. Cubillos, G.I., Romero, E. and Umaña-Perez, A., 2021. ZrN-ZrOxNy vs ZrO2-ZrOxNy coatings deposited via unbalanced DC magnetron sputtering. *Scientific Reports*, *11*(1), pp.1-19.

75. Dettlaff, A., Brodowski, M., Kowalski, M., Stranak, V., Prysiazhnyi, V., Klugmann-Radziemska, E., Ryl, J. and Bogdanowicz, R., 2021. Highly Oriented Zirconium Nitride and Oxynitride Coatings Deposited via High-Power Impulse Magnetron Sputtering: Crystal-Facet-Driven Corrosion Behavior in Domestic Wastewater. *Advanced Engineering Materials*, *23*(7), p.2001349.

76. Geng, M., He, G., Sun, Z., Chen, J., Yang, Z. and Li, Y., 2018. Corrosion damage mechanism of TiN/ZrN nanoscale multilayer anti-erosion coating. *Coatings*, *8*(11), p.400.

77. Stachowiak, G.W. and Batchelor, A.W., 2013. *Engineering tribology*. Butterworth-heinemann.

78. Archard, J., 1953. Contact and rubbing of flat surfaces. *Journal of applied physics*, *24*(8), pp.981-988.